International Journal of Solids and Structures 100–101 (2016) 270–285

Contents lists available at ScienceDirect

International Journal of Solids and Structures

journal homepage: www.elsevier.com/locate/ijsolstr

Numerical analysis on the elastic deformation of the tools in sheet metal forming processes

D.M. Neto[a,*], J. Coër[a,b], M.C. Oliveira[a], J.L. Alves[c], P.Y. Manach[b], L.F. Menezes[a]

[a] CEMUC, Department of Mechanical Engineering, University of Coimbra, Polo II, Rua Luís Reis Santos, Pinhal de Marrocos, 3030-788 Coimbra, Portugal
[b] Univ. Bretagne Sud, FRE CNRS 3744, IRDL, F-56100 Lorient, France
[c] CMEMS, Microelectromechanical Systems Research Unit, University of Minho, Campus de Azurém, 4800-058 Guimarães, Portugal

ARTICLE INFO

Article history:
Received 1 April 2016
Revised 13 July 2016
Available online 28 August 2016

Keywords:
Reverse deep drawing
Tools deformation
Finite element analysis
Material flow
DD3IMP

ABSTRACT

The forming tools are commonly assumed as rigid in the finite element simulation of sheet metal forming processes. This assumption allows to simplify the numerical model and, subsequently, reduce the required computational cost. Nevertheless, the elastic deformation of the tools can influence considerably the material flow, specifically the distribution of the blank-holder pressure over the flange area. This study presents the finite element analysis of the reverse deep drawing of a cylindrical cup, where the forming tools are modelled either as rigid or as deformable bodies. Additionally, the numerical results are compared with the experimental ones, in order to assess the accuracy of the proposed finite element model. Considering the elastic deformation of the tools, the numerical results are in better agreement with the experimental measurements, namely the cup wall thickness distribution. On the other hand, the computational time of the simulation increases significantly in comparison with the classical approach (rigid tools).

1. Introduction

The sheet metal forming processes are commonly used in the automotive industry to produce several body panels. Nevertheless, the high competitively in the current world market has led to a strong reduction of the development periods in the car manufacturing industry (OECD, 2011). Thus, the empirical tool design methods based on trial-and-error procedures has been gradually replaced by the virtual product conception using numerical simulation (Diller et al., 1997; Mario et al., 2013). Indeed, the finite element simulation of sheet metal forming processes is currently used in many companies to predict forming defects, such as necking (or fracture) (Mattiasson et al., 2014; Msolli et al., 2015), springback (Chalal et al., 2012; Ghaei, 2012) or wrinkling (Neto et al., 2015b). The continuous development of these numerical tools over the last 40 years reached an incontestable level of maturity, providing reliable results (Chenot et al., 2014). Nevertheless, in order to decrease the discrepancy between experimental and numerical results, several efforts have been made to improve the accuracy of the numerical models, namely the development of new material constitutive models accounting for both the anisotropy and the kinematic hardening effects (Chen et al., 2016; Lee et al., 2016; Taherizadeh et al., 2015; Yoon et al., 2014).

Typically, the forming tools are assumed as rigid in the finite element simulation of sheet metal forming processes. This allows simplifying the mechanical problem under analysis, specifically the numerical treatment of the frictional contact between the deformable sheet and the tools. However, the actual trend in the automotive industry of increasing application of advanced high strength steels in the bodies-in-white, dictates that the contact forces arising in the forming tools are significantly higher (Xu et al., 2012). Thus, this new paradigm can require the update of the numerical models to incorporate the elastic properties of the tools (Choi et al., 2013; Del Pozo et al., 2007). The adoption of the penalty method with a surface stiffness variable across the surface of the tools provides an approximation for its elastic deformation (Hallquist, 2007). However, the elastic deformation of the tools is governed both by the magnitude of the contact forces arising on its surface, the complete geometry of the tools and its mechanical properties. Therefore, the accurate prediction of the tools deformation requires the modelling of the entire tool geometry (volume instead of surface). Nevertheless, the discretization of the tools with finite elements implies a considerable increase of the computational cost. In order to reduce the number

* Corresponding author. Fax: +351239790701.
E-mail addresses: diogo.neto@dem.uc.pt (D.M. Neto), jeremy.coer@univ-ubs.fr (J. Coër), marta.oliveira@dem.uc.pt (M.C. Oliveira), jlalves@dem.uminho.pt (J.L. Alves), pierre-yves.manach@univ-ubs.fr (P.Y. Manach), luis.menezes@dem.uc.pt (L.F. Menezes).

http://dx.doi.org/10.1016/j.ijsolstr.2016.08.023
0020-7683/

of the degrees of freedom (DOF) involved, and hence the computational cost, the classical static condensation method can be adopted (Hoffmann, 2005), which can be only applicable to linear and small strain problems. Accordingly, only the surface geometry of the tools is discretized (the only of interest for contact analysis), while all internal DOF are eliminated by condensation. An alternative approach is the modal reduction technique, which is based on the calculation of the eigenvalues, where the linear combination of pre-calculated deformation modes leads to the desired final deformation (Lingbeek and Meinders, 2007). This is an approximated method, where the accuracy is defined by the number of deformation modes used (Struck et al., 2008).

Großmann et al. (2009) proposed an iterative method to adjust the shape of the forming tools to compensate its elastic deformation. The results show a significant influence of the tool deflection in the draw-in, mostly due to the distribution of the blank-holder force, which is higher on the die corners (Chen et al., 2012). On the other hand, since the elastic deformation of the tools affects the contact conditions between the sheet and the forming tools, the results presented by Keum et al. (2005) show that the springback prediction is improved when considering the tools deformation in the numerical model. In the study conducted by Doege and Elend (2001), they take advantage of the elastic deflection of the blank-holder to enlarge the safe working area and improve the quality of the produced deep drawing parts. The pliable blank-holder is able to adjust to the changes in sheet thickness occurring during the forming process, providing a uniform pressure distribution in the flange, which improves the material flow.

This study intends to analyse the influence of the tools modelling (rigid or deformable) in the accuracy of the numerical results, namely the contact forces and the thickness distributions. The reverse deep drawing of a cylindrical cup is the example selected, which was proposed as benchmark at the Numisheet'99 conference (Gelin and Picart, 1999). This forming process has been selected due to the process conditions adopted, i.e. the clearance between the die and the blank-holder is kept constant using screws and adjustable washers in-between. Furthermore, typically the multi-stage drawing processes are more difficult to simulate accurately because the stress and strain distributions resulting from the first stage will influence the subsequent behaviour (Thuillier et al., 2002). The organization of the paper is the following: the equations defining the constitutive model of the sheet are recalled in Section 2, while the frictional contact problem is presented in Section 3, considering both the assumption of rigid and deformable forming tools. Both the experimental setup and the developed finite element model of the reverse deep drawing process are described in Section 4, including the comparison between numerical and experimental results, highlighting the influence of the tools deformation in the accuracy of the numerical predictions. The main conclusions of this study are discussed in Section 5.

2. Constitutive model

The constitutive material model establishes the relationships between the most relevant state variables characterizing the continuum medium. In the present study, the deformation of the metallic sheet is described by a rate-independent elastoplastic material model. The material mechanical behaviour is assumed linear and isotropic in the elastic domain and non-linear and anisotropic in the plastic domain (orthotropic plasticity). According to Belytschko et al. (2000), for hypoelastic materials the energy is not conserved in a closed elastic deformation cycle. Nevertheless, assuming that elastic strains are small compared to plastic stains, the adoption of a hypoelastic-plastic model provides an adequate elastic response, with negligible error in the conservation of energy. In this type of constitutive models, the strain rate tensor is decomposed additively by:

$$\mathbf{D} = \mathbf{D}^{\mathrm{e}} + \mathbf{D}^{\mathrm{p}}, \tag{1}$$

where $\mathbf{D}^{\mathrm{e}}$ and $\mathbf{D}^{\mathrm{p}}$ denote the elastic and plastic strain rate tensors, respectively. Thus, the elastic response specified in the differential form is given by:

$$\dot{\boldsymbol{\sigma}} = \mathbf{C}^{\mathrm{e}} : \mathbf{D}^{\mathrm{e}}, \tag{2}$$

where $\dot{\boldsymbol{\sigma}}$ is the Cauchy stress rate (objective derivatives must be used, e.g. Jaumann's derivative) and $\mathbf{C}^{\mathrm{e}}$ denotes the corresponding fourth-order tensor of elastic moduli. The differential form of the constitutive Eq. (2) must satisfy the objectivity condition, which is guaranteed writing the equations in an appropriate orthogonal rotating frame (Dafalias, 1985). The rate of variation of the Cauchy stress tensor according with the Jaumann derivative is defined by:

$$\dot{\boldsymbol{\sigma}}^{\mathrm{J}} = \dot{\boldsymbol{\sigma}} + \boldsymbol{\sigma}\mathbf{W} - \mathbf{W}\boldsymbol{\sigma}, \tag{3}$$

where $\mathbf{W}$ is the total spin tensor (antisymmetric part of the velocity gradient tensor $\mathbf{L}$). Assuming linear isotropic elastic behaviour, the fourth-order tensor of elastic constants is given by:

$$\mathbf{C}^{\mathrm{e}} = \lambda \mathbf{I} \otimes \mathbf{I} + 2\mu \mathbf{I}_4, \tag{4}$$

where λ and μ are the Lamé parameters, $\mathbf{I}$ is the second-order identity tensor and $\mathbf{I}_4$ is the fourth-order identity tensor.

In order to describe the plastic response of the material it is necessary to define: (i) a yield function; (ii) a flow rule and (iii) a hardening law. The yield criterion accounts for the plastic anisotropy of the metallic sheet, bounding the elastic domain. The evolution of the yield surface depends of the hardening law adopted. Indeed, its expansion is dictated by an isotropic hardening law, while its centre translation is dictated by a kinematic hardening law. Thus, the yield condition is defined by the yield criterion and the hardening law through the yield function:

$$\mathcal{F}(\bar{\boldsymbol{\sigma}}, Y) = \bar{\boldsymbol{\sigma}} - Y = 0, \tag{5}$$

where $\bar{\boldsymbol{\sigma}}$ is the equivalent stress and Y denotes the flow stress in simple tension, which depends on the effective plastic strain. The equivalent stress depends of the yield criterion adopted, while the flow stress Y depends of the hardening law adopted. Nevertheless, the equivalent stress is fully defined by the deviator component of the Cauchy stress tensor $\boldsymbol{\sigma}'$, the back-stress tensor $\mathbf{X}$ and the set of internal variables of the considered yield criterion $\boldsymbol{\alpha}$:

$$\bar{\boldsymbol{\sigma}} = \bar{\boldsymbol{\sigma}}(\boldsymbol{\sigma}' - \mathbf{X}, \boldsymbol{\alpha}), \tag{6}$$

where $\boldsymbol{\sigma}' - \mathbf{X}$ denotes the effective deviatoric stress tensor. The back-stress tensor $\mathbf{X}$ is a deviatoric, symmetric second-order tensor, which depends of the kinematic hardening law adopted. The adopted constitutive model considers an associated inviscid flow rule, which defines the direction of the plastic strain rate through the gradient of the yield function:

$$\mathbf{D}^{\mathrm{p}} = \dot{\lambda}\mathbf{V} = \dot{\lambda}\frac{\partial \mathcal{F}}{\partial(\boldsymbol{\sigma}' - \mathbf{X})}, \tag{7}$$

where $\dot{\lambda}$ denotes the plastic multiplier and $\mathbf{V}$ is the first derivative of the yield condition in order to the effective deviatoric stress tensor (Menezes and Teodosiu, 2000). The plastic multiplier is determined by enforcing the consistency condition:

$$\dot{\mathcal{F}} = \frac{\partial \mathcal{F}}{\partial \boldsymbol{\sigma}} : \dot{\boldsymbol{\sigma}} + \frac{\partial \mathcal{F}}{\partial \boldsymbol{\alpha}} : \dot{\boldsymbol{\alpha}} = 0, \tag{8}$$

where $\dot{\mathcal{F}}$ is the time derivative of the yield condition (5). In the present study, the isotropic work hardening behaviour, which describes the evolution of the flow stress with plastic work, is modelled by the Swift law:

$$Y = K(\varepsilon_0 + \bar{\varepsilon}^{\mathrm{p}})^n \quad \text{with} \quad \varepsilon_0 = \left(\frac{Y_0}{K}\right)^{1/n}, \tag{9}$$

where K, ε_0 and n are the material parameters, while $\bar{\varepsilon}^p$ denotes the equivalent plastic strain and Y_0 denotes the initial value of the yield stress. The slope of the hardening curve is defined by the plastic modulus:

$$H' = \partial Y / \partial \bar{\varepsilon}^p, \tag{10}$$

which depends on the adopted hardening law (9). The consistency condition (8) can be rewritten considering generic expressions for the isotropic hardening law and of the yield criterion:

$$\dot{\mathcal{F}} = \mathbf{V} : (\dot{\boldsymbol{\sigma}} - \dot{\mathbf{X}}) - H' \dot{\bar{\varepsilon}}^p = 0, \tag{11}$$

where $\dot{\bar{\varepsilon}}^p$ denotes the equivalent plastic strain rate, such that $\dot{\bar{\varepsilon}}^p = \dot{\lambda}$.

The amount of springback predicted by the numerical simulation is strongly affected by the Bauschinger effect (Chun et al., 2002), which is numerically described by means of the kinematic hardening concept introduced by Prager (1949). The kinematic part of the work hardening, i.e. the non-linear evolution of the back-stress tensor $\mathbf{X}$, is described by the non-linear law with saturation proposed by Frederick and Armstrong (2007), given by:

$$\dot{\mathbf{X}} = C_X \left[\frac{X_{sat}}{\bar{\sigma}} (\boldsymbol{\sigma}' - \mathbf{X}) - \mathbf{X} \right] \dot{\bar{\varepsilon}}^p \quad \text{with} \quad \mathbf{X}(0) = \mathbf{0}, \tag{12}$$

where X_{sat} characterizes the saturation value of $\mathbf{X}$, while the material parameter C_X characterizes the rate of approaching the saturation. This evolution law is widely used to describe the back stress's evolution, since it provides accurate predictions of the Bauschinger effect (Grilo et al., 2016).

2.1. Anisotropic yield function

The rolling operation used in the manufacture of metallic sheets induces anisotropy in the mechanical properties. In order to model this behaviour of the metallic sheet, the Hill's quadratic yield function have been considered (Hill, 1948), which is widely used in the sheet metal forming simulation of steels (Dasappa et al., 2012). The extension of the isotropic von Mises yield criterion to anisotropy proposed by Hill (1948) is given by:

$$\bar{\sigma}^2 = (\boldsymbol{\sigma}' - \mathbf{X}) : \mathbf{M} : (\boldsymbol{\sigma}' - \mathbf{X}), \tag{13}$$

where $\bar{\sigma}$ is the equivalent stress and $\mathbf{M}$ denotes the fourth-order symmetric tensor, which takes into account the orthotropic symmetry of the material. Due to the incompressible character of plasticity, the yield criterion depends only of the effective deviatoric stress tensor $\boldsymbol{\sigma}' - \mathbf{X}$, where $\boldsymbol{\sigma}'$ is the deviator of the Cauchy stress tensor and $\mathbf{X}$ is the back-stress tensor. The parameters that describe the anisotropy of the material, i.e. the variation in the yield stress and the r-values with the in-plane orientation, are contained in the definition of this tensor. Accordingly, the Hill'48 yield criterion, defined in the appropriate orthogonal rotating frame, is given by:

$$\begin{aligned} \bar{\sigma}^2 = {} & F(\sigma'_{22} - X_{22} - \sigma'_{33} + X_{33})^2 + G(\sigma'_{33} - X_{33} - \sigma'_{11} + X_{11})^2 \\ & + H(\sigma'_{11} - X_{11} - \sigma'_{22} + X_{22})^2 + \\ & + 2L(\sigma_{23} - X_{23})^2 + 2M(\sigma_{13} - X_{13})^2 + 2N(\sigma_{12} - X_{12})^2, \end{aligned} \tag{14}$$

where F, G, H, L, M and N are the parameters that describe the anisotropy of the material. σ'_{11}, σ'_{22} and σ'_{33} denote the deviatoric Cauchy stress components in the rolling, transverse and thickness directions, respectively, while σ_{12}, σ_{23} and σ_{13} are the shear stresses in the three orthogonal directions respectively. According with (7), the associated flow rule for the Hill'48 yield function (13) can be written as:

$$\mathbf{D}^p = \dot{\lambda} \frac{\mathbf{M} : (\boldsymbol{\sigma}' - \mathbf{X})}{\bar{\sigma}}, \tag{15}$$

which defines the direction of the plastic strain rate. The second-order derivative of the quadratic anisotropic yield criterion (Hill'48) in order to the effective deviatoric stress tensor, is given by:

$$\mathbf{Q} = \frac{\partial^2 \bar{\sigma}}{\partial (\boldsymbol{\sigma}' - \mathbf{X})^2} = \frac{\mathbf{M}\bar{\sigma} - (\mathbf{M} : (\boldsymbol{\sigma}' - \mathbf{X})) \otimes \mathbf{V}}{\bar{\sigma}^2}. \tag{16}$$

2.2. Time integration

The implementation of the combined isotropic and kinematic hardening laws previously described into an implicit finite element code is briefly outlined. The time integration of the constitutive law allows to evaluate, in each point, the equivalent plastic strain increment, the new stress state tensor and all state variables dependent on these two quantities. The hypoelastic-plastic constitutive model for large strain can be written in the form of a linear relation between the objective measures of the stress rate and the strain rate:

$$\dot{\boldsymbol{\sigma}}^J = \mathbf{C}^{ep} : \mathbf{D}, \tag{17}$$

where $\mathbf{C}^{ep}$ is a fourth-order tensor that defines the elastoplastic modulus. The expression for this tensor depends of the algorithms adopted in the integration of the constitutive model and on the type of relation considered between the states at the beginning and at the end of the loading increment. Thus, it is possible to consider the tangent elastoplastic modulus or the consistent elastoplastic modulus (Alves, 2003).

The tangent elastoplastic modulus establishes the relationship between the Cauchy stress rate tensor and the strain rate tensor, defined as:

$$\mathbf{C}^{ep}_{tan} = \mathbf{C}^e - \alpha f_0 \mathbf{V} \otimes \mathbf{V}, \tag{18}$$

where α takes the value 0 in the elastic domain, while for an elastoplastic increment its value is equal to 1. The parameter f_0 depends on the isotropic and kinematic hardening laws adopted. For the Frederick-Armstrong law is given by:

$$f_0 = \frac{4\mu^2}{2\mu \mathbf{V} : \mathbf{V} + C_X \mathbf{V} : \left[\frac{X_{sat}}{\bar{\sigma}} (\boldsymbol{\sigma}' - \mathbf{X}) - \mathbf{X} \right] + H'}, \tag{19}$$

where $\mathbf{V}$ and H' are given explicitly by (15) and (10), respectively (Alves et al., 2007).

The consistent elastoplastic modulus establishes the relationship between the incremental Cauchy stress tensor and the incremental strain tensor for a given time increment. The backward Euler time integration algorithm is commonly adopted (Grilo et al., 2016), which uses the time derivatives at the end of the increment (Simo and Taylor, 1985). The temporal integration of the elastic response (differential form specified in (2)) over the abovementioned time interval Δt allows to evaluate the stress increment as:

$$\boldsymbol{\sigma}_f - \boldsymbol{\sigma}_0 = \mathbf{C}^e : \Delta \boldsymbol{\varepsilon}^e = \mathbf{C}^e : (\Delta \boldsymbol{\varepsilon} - \Delta \boldsymbol{\varepsilon}^p), \tag{20}$$

where the subscripts f and 0 are used to refer the quantities at the end and at the beginning of time increment, respectively. The total strain tensor increment $\Delta \varepsilon$ and the plastic strain increment $\Delta \varepsilon^p$ are calculated by means of integration of the total and plastic strain rate tensors, over the time increment Δt. Integrating the adopted kinematic hardening law (12) in the same time increment and subtracting the result to (20), it can be written:

$$\begin{aligned} \boldsymbol{\sigma}_f - \mathbf{X}_f = {} & \boldsymbol{\sigma}_0 - \mathbf{X}_0 + 2\mu \Delta \boldsymbol{\varepsilon} - 2\mu \Delta \boldsymbol{\varepsilon}^p \\ & - \left[\frac{X_{sat}}{\bar{\sigma}} (\boldsymbol{\sigma}'_f - \mathbf{X}_f) - \mathbf{X}_0 \right] (1 - e^{-C_X \Delta \bar{\varepsilon}^p}), \end{aligned} \tag{21}$$

where the plastic strain increment is given by the middle point rule using a fully implicit approximation (Hughes and Winget, 1980):

$$\Delta \boldsymbol{\varepsilon}^p = \Delta \lambda \mathbf{V}_f. \tag{22}$$

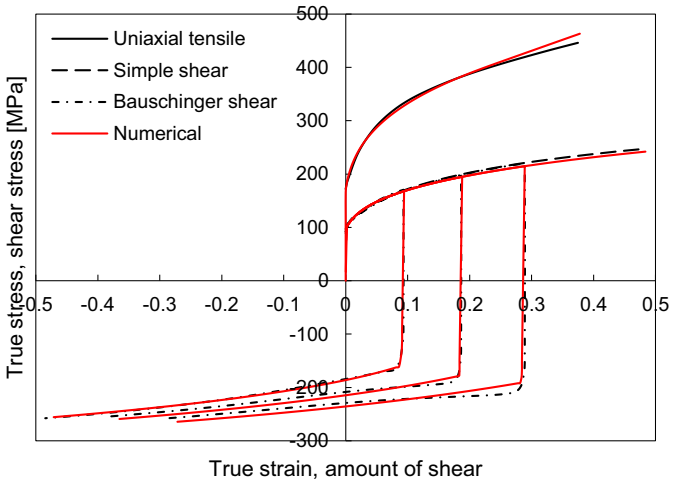

Fig. 1. Comparison of the stress–strain curves predicted by the constitutive model with the experimental ones for uniaxial tensile test, monotonic simple shear and reversed simple shear tests after 10%, 20% and 30% forward shearing.

The linearization of (21) in the vicinity of the final configuration allows to define the consistent elastoplastic modulus for the kinematic hardening law adopted as (for an arbitrary isotropic hardening law and yield criterion):

$$\mathbf{C}_{\text{con}}^{\text{ep}} = \mathbf{C}^{\text{e}} - 4\mu^2(1-\beta)\left(\frac{\mathbf{V}_{\text{f}}\otimes\mathbf{V}_{\text{f}}}{H'_{\text{f}}} + \Delta\bar{\varepsilon}^{\text{p}}\mathbf{Q}_{\text{f}}\right)\mathbf{\Lambda}, \tag{23}$$

where the parameter β is used to decompose the strain increment into the elastic and elastoplastic components that occur over the time increment Δt. The tensor $\mathbf{\Lambda}$ depends on the kinematic hardening law adopted in the constitutive model, being defined for the Frederick-Armstrong law by:

$$\mathbf{\Lambda}^{-1} = \frac{\bar{\sigma} + X_{\text{sat}}\left(1-e^{-C_{\text{X}}\Delta\bar{\varepsilon}^{\text{p}}}\right)}{\bar{\sigma}}\mathbf{I}_4 + 2\mu\left(\frac{\mathbf{V}_{\text{f}}\otimes\mathbf{V}_{\text{f}}}{H'_{\text{f}}} + \Delta\bar{\varepsilon}^{\text{p}}\mathbf{Q}_{\text{f}}\right) + \\ + \frac{C_{\text{X}}e^{-C_{\text{X}}\Delta\bar{\varepsilon}^{\text{p}}}}{H'_{\text{f}}}\left(\frac{X_{\text{sat}}}{\bar{\sigma}}(\boldsymbol{\sigma}'_{\text{f}} - \mathbf{X}_{\text{f}}) - \mathbf{X}_0\right)\otimes\mathbf{V}_{\text{f}}, \tag{24}$$

where $\mathbf{Q}$ represents the second-order derivative of the yield criterion in order to the effective deviatoric stress tensor, given in (16) for the Hill'48 yield criterion (Alves et al., 2007).

2.3. Material parameters identification

The deep drawing quality (DDQ) mild steel is the material selected for the blank. The elastic behaviour is assumed isotropic and constant, which is described by the Hooke's law with Young's modulus of 210 GPa and Poisson ratio of 0.30. Regarding the plastic response, the constitutive parameters of the hardening law (isotropic and kinematic) and yield criterion (associated flow rule) are calculated from experimental tests (Thuillier et al., 2010). The material parameters are identified by the best fit to the experimental values, minimizing a cost function using least squares estimation.

The identification procedure adopted for the material parameters involved in the hardening laws has been detailed by Haddadi et al. (2006). The set of experimental tests used is: (i) uniaxial tensile test along the rolling direction up to localized necking; (ii) monotonic simple shear tests along the rolling direction up to 50% amount of shear and (iii) Bauschinger simple shear tests along the rolling direction, after 10%, 20% and 30% amount of monotonic shear. The experimental stress–strain curve of each above mentioned test is presented in Fig. 1. The procedure used to identify the best set of constitutive parameters is based on the minimization of an error function that evaluates the difference between the predicted and the experimental stress values (Dasappa et al., 2012). Accordingly, the optimization problem consists in determining the set of material parameters **A**, which minimizes the following cost function:

$$F(\mathbf{A}) = \sum_{i=1}^{n_{\text{t}}}\frac{1}{m_i}\sum_{j=1}^{m_i}\left(w_{ij}\left(\frac{\sigma_{ij}^{\text{sim}}}{\sigma_{ij}^{\text{exp}}} - 1\right)^2\right), \tag{25}$$

where n_{t} is the number of different tests, m_i is the number of measured points of the ith test, σ denotes the tensile or shear stress and w is the weight associated with each stress point. In the present study the weighting factors are considered equal to 1. The superscripts "sim" and "exp" denote the simulation and experimental data, respectively. The obtained material parameters for the isotropic hardening described by the Swift law (9) and the non-linear kinematic hardening defined by the Frederick-Armstrong law (12) are listed in Table 1. The inclusion of the non-linear kinematic hardening improves the accuracy of the sheet metal forming simulation, when the plastic deformation occurs in cyclic loading paths (Taherizadeh et al., 2015). The comparison between experimental and numerical stress–strain curves is also presented in Fig. 1. The adopted constitutive model allows describing accurately the mechanical behaviour of the mild steel. Indeed, both the monotonic and cyclic stress–strain curves obtained by the numerical model are in good agreement with the experimental ones, although the model does not allow to describe the work hardening stagnation (Yoshida and Uemori, 2002).

Table 1
Material parameters for the isotropic–kinematic hardening described by Swift law.

Y_0[MPa]	K[MPa]	n	C_{X}	X_{sat}[MPa]
172.0	500.8	0.20	2.2	68.2

Table 2
Anisotropy parameters for the Hill'48 yield criterion.

F	G	H	L	M	N
0.314	0.366	0.634	1.500	1.500	1.176

The orthotropic behaviour of the mild steel (DDQ) is described in the present study by the classical Hill'48 yield criterion. The most common method of determining the parameters of Hill'48 yield criterion is based on the Lankford coefficients (Dasappa et al., 2012). Accordingly, the anisotropy parameters are evaluated through the following relations:

$$\frac{H}{G} = r_0; \quad \frac{F}{G} = \frac{r_0}{r_{90}}; \quad \frac{N}{G} = \left(r_{45} + \frac{1}{2}\right)\left(\frac{r_0}{r_{90}} + 1\right), \tag{26}$$

where r_0, r_{45} and r_{90} are the r-values obtain'ed experimentally by uniaxial tensile tests carried out along 0°, 45° and 90° to the rolling direction (Thuillier et al., 2010). Since the identification of the material parameters for the hardening law (see Table 1) was carried out using the stress–strain curves obtained for specimens oriented along the rolling direction (RD), the yield stress value considered in the identification of the yield criterion parameters corresponds to the one obtained for the uniaxial tensile test performed with the specimen oriented along RD (Neto et al., 2014a). Therefore, the condition $G+H=1$ is introduced in order to evaluate the parameters F, G, H and N. The identified anisotropy parameters of the Hill'48 yield criterion are presented in Table 2. The sheet is assumed isotropic through the thickness, leading to $L=M=1.5$. The in-plane evolution of the r-value predicted by the Hill'48 yield criterion is presented in Fig. 2, which is compared with the experimental values. Furthermore, the uniaxial yield stress values pre-

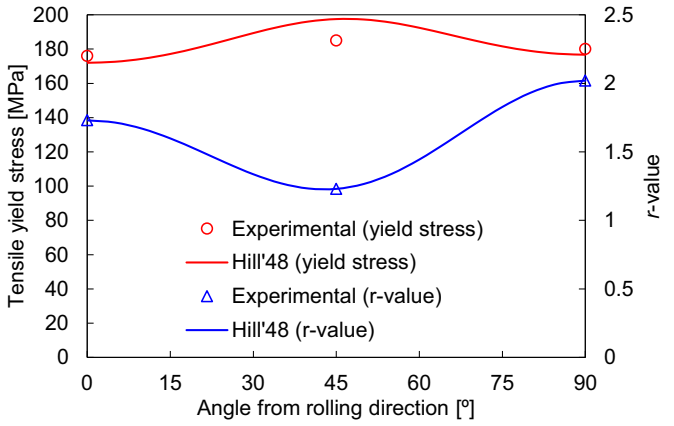

Fig. 2. Tensile yield stress and r-value in the sheet's plane for the DDQ mild steel: comparison between the experimental values and the ones obtained considering the Hill'48 yield criterion.

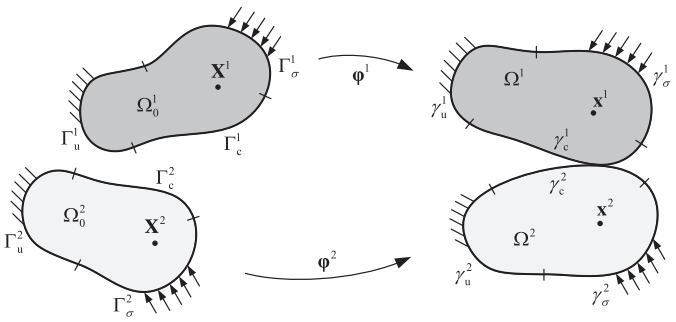

Fig. 3. Notation adopted in the definition of the two-body frictional contact problem undergoing finite deformation.

dicted for different orientations with RD are also presented and compared with the experimental values.

3. Contact mechanics

The numerical simulation of sheet metal forming processes requires the definition of the frictional contact conditions between the forming tools and the metallic sheet. Since the stiffness of the forming tools is significantly larger than the one of the blank, they are usually assumed as rigid in the numerical model, allowing to simplify the problem formulation (Heege and Alart, 1996). Nevertheless, all contact problems are inherently non-linear since the contacting surface on which the loads are transferred from one body to another is unknown *a priori*.

3.1. Contact constraints

The formulation for 3D contact problems undergoing finite deformation and large sliding is briefly summarized. Considering a two-body frictional contact problem, as illustrated in Fig. 3, the current configuration of each body Ω^i is obtained by applying the deformation mapping $\boldsymbol{\varphi}^i$ to the reference configuration Ω_0^i. The superscript $i=1$ and $i=2$ indicates body 1 and body 2, respectively. The boundaries of the two bodies in the current configuration are divided into three disjoint sets: γ_{u}^i, γ_σ^i and γ_{c}^i denoting the Dirichlet boundary (prescribed displacements), Neumann boundary (prescribed traction) and the potential contact boundary, respectively.

In order to define the fundamental kinematic and static variables of the contact problem, the body 1 is referred as the slave body (slave surface γ_{c}^1) and the body 2 is referred as the master body (master surface γ_{c}^2). The normal gap function expressed for any material point on the slave surface $\mathbf{x}^{\mathrm{s}} \in \gamma_{\mathrm{c}}^1$ is defined as follows:

$$g_{\mathrm{n}} = (\mathbf{x}^{\mathrm{s}} - \bar{\mathbf{x}}^{\mathrm{m}}) \cdot \bar{\mathbf{n}}, \tag{27}$$

where $\bar{\mathbf{n}}$ denotes the current outward normal vector on the master surface at the projection point $\bar{\mathbf{x}}^{\mathrm{m}}$, evaluated according to the closest point projection of the slave point onto the master surface (Konyukhov and Schweizerhof, 2008). Accordingly, the value of the normal gap function is negative when the slave point is penetrating the master body, which is physically inadmissible (Pietrzak and Curnier, 1999). For sake of simplicity, all quantities evaluated at the projection point are denoted by a bar over it. The change of the closest point projection defines the relative tangential sliding between contact surfaces. Thus, the tangential slip vector is given as follows:

$$\mathbf{g}_{\mathrm{t}} = \bar{\tau}_\alpha \dot{\xi}^\alpha, \tag{28}$$

where $\boldsymbol{\tau}_\alpha$ denotes the covariant tangential basis vectors on the parameterized master surface, evaluated at the projection point, while $\boldsymbol{\xi} = (\xi^1, \xi^2)$ are the convective coordinates of the parameterized master surface (Laursen and Simo, 1993).

Considering the local linear momentum balance across the contact interface, the action–reaction principle must be satisfied in each contact point, i.e. the contact force exercised by the slave body on the master surface is equal and opposite to the one applied by the master body on the slave surface. Analogously to the kinematic variables, the contact traction acting on the master surface is decomposed into normal and tangential components:

$$\mathbf{t} = p_{\mathrm{n}}\mathbf{n} + \mathbf{t}_{\mathrm{t}}, \tag{29}$$

where p_{n} denotes the normal contact pressure.

The contact constraints in the normal direction are imposed through the unilateral contact conditions, which define the physical requirements of impenetrability and compressive interaction between the bodies. These contact constraints are known as the Hertz–Signorini–Moreau conditions:

$$g_{\mathrm{n}} \geq 0; \quad p_{\mathrm{n}} \leq 0; \quad p_{\mathrm{n}} g_{\mathrm{n}} = 0, \tag{30}$$

where the first indicates the impenetrability constraint, the second imposes that the normal contact traction is compressive and the last is the complementarity condition between the first two conditions. Assuming the classical non-associated Coulomb's friction law at the contact interface, the contact constraints associated with the friction law are given as follows:

$$\|\mathbf{t}_{\mathrm{t}}\| - \mu|p_{\mathrm{n}}| \leq 0; \quad \mathbf{t}_{\mathrm{t}} - \mu|p_{\mathrm{n}}|\frac{\mathbf{g}_{\mathrm{t}}}{\|\mathbf{g}_{\mathrm{t}}\|} = \mathbf{0}; \quad \|\mathbf{g}_{\mathrm{t}}\|(\|\mathbf{t}_{\mathrm{t}}\| - \mu|p_{\mathrm{n}}|) = 0, \tag{31}$$

where μ denotes the coefficient of friction. The first condition indicates the stick/slip contact status, i.e. imposes that the magnitude of the friction force does not exceed the contact pressure multiplied by the friction coefficient. The second condition indicates the slip rule, which defines that the friction force vector is collinear with the tangential slip vector. The last condition is the complementarity condition between the first two conditions (Mijar and Arora, 2000).

The nonlinear boundary value problem (BVP) for the frictional contact system undergoing finite deformation, shown in Fig. 3, is stated as follows:

$$\begin{cases} \mathrm{div}(\boldsymbol{\sigma}^i) + \mathbf{b}^i = \mathbf{0}, & \text{in } \Omega^i \\ \mathbf{t}^i = \boldsymbol{\sigma}^i \mathbf{n}^i = \bar{\mathbf{t}}^i, & \text{on } \gamma_\sigma^i \\ \mathbf{u}^i = \bar{\mathbf{u}}^i, & \text{on } \gamma_{\mathrm{u}}^i \end{cases}, \tag{32}$$

where $\boldsymbol{\sigma}^i$ denotes the Cauchy stress tensor (inertia terms are neglected). Furthermore, the bodies are only subject to body forces $\mathbf{b}^i$ and prescribed boundary conditions, namely applied boundary

tractions $\bar{\mathbf{t}}^i$ on the Neumann boundary and prescribed displacements $\bar{\mathbf{u}}^i$ on the Dirichlet boundary. Accordingly, the strong form of the two-body frictional contact problem is defined in (32), considering the contact constraints given in (30) and (31). The weak formulation of the BVP is obtained using the principle of virtual velocities proposed by McMeeking and Rice (1975).

3.2. Augmented lagrangian method

The frictional contact problem is regularized with the augmented Lagrangian method, originally proposed by Alart and Curnier (1991) to deal with frictional contact problems. This method allows an exact enforcement of the contact constraints defined through relations (30) and (31), while providing a smooth functional (Pietrzak and Curnier, 1999). Therefore, the minimization problem with inequality constraints is converted into a fully unconstrained one, where the solution is the saddle point of a functional (minimize primal variables and maximize dual variables). In the present implementation, the Lagrange multipliers are retained as independent variables in the coupled problem, i.e. both variables are updated simultaneously in a single loop. This strategy has also been adopted by other authors as e.g. Cavalieri and Cardona (2015).

The augmented Lagrangian functional only related with frictional contact contribution can be written as:

$$\mathcal{L}^{\mathrm{c}}(\mathbf{u},\boldsymbol{\lambda}) = g_{\mathrm{n}}\lambda_{\mathrm{n}} + \frac{\varepsilon}{2}|g_{\mathrm{n}}|^2 - \frac{1}{2\varepsilon}\mathrm{dist}^2(\hat{\lambda}_{\mathrm{n}}, \Re^-) + \mathbf{g}_{\mathrm{t}}\cdot\boldsymbol{\lambda}_{\mathrm{t}} + \frac{\varepsilon}{2}\|\mathbf{g}_{\mathrm{t}}\|^2 - \frac{1}{2\varepsilon}\mathrm{dist}^2(\hat{\boldsymbol{\lambda}}_{\mathrm{t}}, C^{\mathrm{augm}}), \tag{33}$$

where ε denotes the penalty parameter and dist(x, C) is the distance between x and C. The Lagrange multipliers λ_{n} and $\boldsymbol{\lambda}_{\mathrm{t}}$ represent the normal contact force and the friction force, respectively. Hence, the augmented Lagrange multiplier, denoted by a hat, is defined as:

$$\hat{\boldsymbol{\lambda}} = \hat{\lambda}_{\mathrm{n}}\mathbf{n} + \hat{\boldsymbol{\lambda}}_{\mathrm{t}} = (\lambda_{\mathrm{n}} + \varepsilon g_{\mathrm{n}})\mathbf{n} + (\boldsymbol{\lambda}_{\mathrm{t}} + \varepsilon\mathbf{g}_{\mathrm{t}}), \tag{34}$$

which is decomposed into the normal and tangential components. The extended cone C^{augm} is the convex set defined by extension of the friction cone to the positive half-line $\Re^+$, i.e. the set of positive values of the normal augmented Lagrange multiplier (Alart and Curnier, 1991).

The solution of the frictional contact problem is obtained through the variation of the augmented Lagrangian functional. This leads to a mixed system of nonlinear equations involving both nodal displacements and contact forces as unknowns. The extension of the Newton–Raphson method to non-differentiable problems arising from contact mechanics was investigated by Alart (1997) and Heegaard and Curnier (1993), developing the generalized Newton method. The main idea of this method is to split the system of nonlinear equations into two parts, i.e. a differentiable structural part $\mathcal{F}^{\mathrm{s}}$ and a non-differentiable contact part $\mathcal{F}^{\mathrm{c}}$ such that:

$$\mathcal{F}(\mathbf{u},\boldsymbol{\lambda}) = \mathcal{F}^{\mathrm{s}}(\mathbf{u}) + \mathcal{F}^{\mathrm{c}}(\mathbf{u},\boldsymbol{\lambda}) = \mathbf{0}, \tag{35}$$

where $\mathcal{F}^{\mathrm{s}}$ represents the virtual work of the two-body system in absence of contact and $\mathcal{F}^{\mathrm{c}}$ denotes the virtual work due to the frictional contact forces, i.e. the variation of the augmented Lagrangian functional defined in (33). Accordingly, the application of the generalized Newton method is stated as:

$$\begin{bmatrix} \nabla_{\mathbf{u}}\mathcal{F}^{\mathrm{s}}(\mathbf{u}_i) + \nabla_{\mathbf{u}}\mathcal{F}^{\mathrm{c}}(\mathbf{u}_i,\boldsymbol{\lambda}_i) \\ \nabla_{\boldsymbol{\lambda}}\mathcal{F}^{\mathrm{c}}(\mathbf{u}_i,\boldsymbol{\lambda}_i) \end{bmatrix} \begin{Bmatrix} \Delta\mathbf{u}_i \\ \Delta\boldsymbol{\lambda}_i \end{Bmatrix} = -\left\{\mathcal{F}^{\mathrm{s}}(\mathbf{u}_i) + \mathcal{F}^{\mathrm{c}}(\mathbf{u}_i,\boldsymbol{\lambda}_i)\right\}, \tag{36}$$

where i is the iteration index and $\nabla_{\mathbf{u}}\mathcal{F}^{\mathrm{s}}$ denotes the tangent matrix of the contacting bodies. The sub-gradients $\nabla_{\mathbf{u}}\mathcal{F}^{\mathrm{c}}$ and $\nabla_{\boldsymbol{\lambda}}\mathcal{F}^{\mathrm{c}}$ are components of the generalized Jacobian matrices for primal and dual variables. Thus, a different Jacobian matrix is derived according to the contact status (gap, stick or slip) of the node (Heege and Alart, 1996; Neto et al., 2016).

3.3. Node-to-segment contact elements

The node-to-segment discretization technique, widely used in contact problems undergoing finite deformation and large sliding (Zavarise and De Lorenzis, 2009), is adopted in the present study. It is associated with the *master–slave* approach (Hallquist et al., 1985), dictating the enforcement of the contact constraints (unilateral contact condition and friction law) only in the slave nodes. Consequently, each contact element is composed by a slave node and the corresponding segment on the master surface, as shown in Fig. 4. Since the frictional contact constraints are treated with the augmented Lagrangian method, each contact element is complemented by an artificial node to store the contact force (Lagrange multipliers). Nevertheless, the transmission of the contact forces through the contact interface only occurs for contact between deformable bodies (Neto et al., 2015). The approximation of the stiffer contacting body by a rigid surface does not requires the spatial discretization of the body, thus no additional degrees of freedom are involved. In order to improve the accuracy and robustness of the numerical simulation, in the present study the master surface is smoothed with Nagata patches (Neto et al., 2016, 2014b).

In analogy to the internal forces of a classical finite element, the internal force vector for a single contact element derived from the augmented Lagrangian method (Cavalieri and Cardona, 2015; Heege and Alart, 1996) is defined by:

$$\mathbf{F}^{\mathrm{c}}(\mathbf{u},\boldsymbol{\lambda}) = \begin{Bmatrix} \mathrm{proj}_{\Re^-}\left(\hat{\lambda}_{\mathrm{n}}\right)\mathbf{n} + \mathrm{proj}_{C^{\mathrm{augm}}}\left(\hat{\boldsymbol{\lambda}}_{\mathrm{t}}\right) \\ -\left\{\mathrm{proj}_{\Re^-}\left(\hat{\lambda}_{\mathrm{n}}\right)\mathbf{n} + \mathrm{proj}_{C^{\mathrm{augm}}}\left(\hat{\boldsymbol{\lambda}}_{\mathrm{t}}\right)\right\} \\ -1/\varepsilon\left\{\lambda_{\mathrm{n}} - \mathrm{proj}_{\Re^-}\left(\hat{\lambda}_{\mathrm{n}}\right)\right\}\mathbf{n} - 1/\varepsilon\left\{\boldsymbol{\lambda}_{\mathrm{t}} - \mathrm{proj}_{C^{\mathrm{augm}}}\left(\hat{\boldsymbol{\lambda}}_{\mathrm{t}}\right)\right\} \end{Bmatrix}, \tag{37}$$

where the first line is connected with the slave node, the second one represents all nodes composing the master segment, while the last one presents the additional equations necessary to evaluate the frictional contact forces (in the slave node). In case of contact with a rigid obstacle, the contact forces arising in the slave nodes are not transferred to the master surface, leading to a simpler form of the residual vector, i.e. the second line of (37) vanish (Heege and Alart, 1996).

The elemental contribution of a contact element to the global right-hand side vector of the equilibrium equations depends on the contact status (gap, stick or slip). The gap status (absence of contact) is defined by the normal component of the augmented Lagrange multiplier through the condition $\hat{\lambda}_{\mathrm{n}} > 0$. In this case, $\mathrm{proj}_{\Re^-}(\hat{\lambda}_{\mathrm{n}}) = 0$ and $\mathrm{proj}_{C^{\mathrm{augm}}}(\hat{\boldsymbol{\lambda}}_{\mathrm{t}}) = \mathbf{0}$, where the contribution of this contact element to the internal contact force vector yields:

$$\mathbf{F}^{\mathrm{c}}_{\mathrm{gap}}(\mathbf{u},\boldsymbol{\lambda}) = \begin{Bmatrix} \mathbf{0} \\ \mathbf{0} \\ -\boldsymbol{\lambda}/\varepsilon \end{Bmatrix}. \tag{38}$$

The stick contact status is defined by the condition $\|\hat{\boldsymbol{\lambda}}_{\mathrm{t}}\| < -\mu\hat{\lambda}_{\mathrm{n}}$, leading to $\mathrm{proj}_{\Re^-}(\hat{\lambda}_{\mathrm{n}}) = \hat{\lambda}_{\mathrm{n}}$ and $\mathrm{proj}_{C^{\mathrm{augm}}}(\hat{\boldsymbol{\lambda}}_{\mathrm{t}}) = \hat{\boldsymbol{\lambda}}_{\mathrm{t}}$. Therefore, from (37) the contribution to the internal contact force vector yields:

$$\mathbf{F}^{\mathrm{c}}_{\mathrm{stick}}(\mathbf{u},\boldsymbol{\lambda}) = \begin{Bmatrix} \hat{\lambda}_{\mathrm{n}}\mathbf{n} + \hat{\boldsymbol{\lambda}}_{\mathrm{t}} \\ -(\hat{\lambda}_{\mathrm{n}}\mathbf{n} + \hat{\boldsymbol{\lambda}}_{\mathrm{t}}) \\ g_{\mathrm{n}}\mathbf{n} + \mathbf{g}_{\mathrm{t}} \end{Bmatrix}. \tag{39}$$

Finally, the slip status is defined by the condition $\|\hat{\boldsymbol{\lambda}}_{\mathrm{t}}\| \geq -\mu\hat{\lambda}_{\mathrm{n}}$, leading to $\mathrm{proj}_{\Re^-}(\hat{\lambda}_{\mathrm{n}}) = \hat{\lambda}_{\mathrm{n}}$ and $\mathrm{proj}_{C^{\mathrm{augm}}}(\hat{\boldsymbol{\lambda}}_{\mathrm{t}}) = \mu\hat{\lambda}_{\mathrm{n}}\mathbf{t}$. Then, the

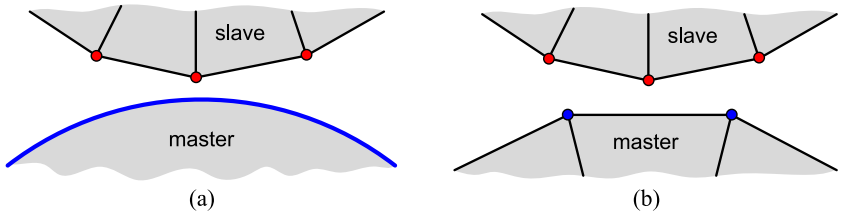

Fig. 4. Graphical representation of the node-to-segment contact discretization considering the master body: (a) rigid; (b) deformable.

contribution of this contact element to the internal contact force vector is given by:

$$\mathbf{F}^{c}_{slip}(\mathbf{u},\boldsymbol{\lambda}) = \begin{Bmatrix} \hat{\lambda}_n(\mathbf{n}-\mu\mathbf{t}) \\ -(\hat{\lambda}_n(\mathbf{n}-\mu\mathbf{t})) \\ g_n\mathbf{n}-(\boldsymbol{\lambda}_t+\mu\hat{\lambda}_n\mathbf{t})/\varepsilon \end{Bmatrix}, \tag{40}$$

where the tangential slip direction unit vector is defined by:

$$\mathbf{t} = \hat{\boldsymbol{\lambda}}_t/\|\hat{\boldsymbol{\lambda}}_t\|. \tag{41}$$

The Jacobian matrices associated to the internal force vector (37) were derived by Neto et al. (2016) for each contact status (gap, stick or slip). The pattern of nonzero entries in the global tangent matrix is symmetric. Nevertheless, the pattern needs to be update in large sliding contact problems, which is computationally expensive. On the other hand, the global tangent matrix presents a fixed pattern when the master surface is assumed rigid (Neto et al., 2015).

4. Reverse deep drawing

In order to accomplish high drawing ratios in the deep drawing process, it is usually decomposed into several forming stages. The reverse deep drawing of a cylindrical cup, proposed at the Numisheet'99 conference, is the forming process selected in this study (Gelin and Picart, 1999). This deep drawing process is characterized by the change of the drawing direction from the first to the second stage, i.e. the punch travels in the reverse direction during the second stage. The deep drawing quality (DDQ) mild steel is the material selected for the blank, which has 170 mm of initial diameter and 0.98 mm in thickness.

4.1. Experimental setup

The experimental drawing device was developed by Thuillier et al. (2002) in order to be attached at the connecting ends of a classical tensile test machine. The apparatus of the first stage is composed by a hollow punch of 100 mm external diameter, a die with an internal diameter of 104.5 mm and a blank-holder (see Fig. 5(a)). In order to impose a fixed initial gap between the blank-holder and the die, the tools are connected by means of eight screws and adjustable washers put in-between, as shown in Fig. 5(a). An identical procedure is adopted in the second stage, where the blank-holder is connected to the die by means of a hat-shaped part, as shown in Fig. 5(b). Note that the punch of the first stage becomes the die of the second forming stage, as highlighted in Fig. 5. The main dimensions of the forming tools are given in Table 3.

The punch involved in each forming stage was built in hardened tool steel while the other tools and connection parts were made of high strength steel. All surfaces of the forming tools with the possibility to establish contact with the blank are heat treated and ground to obtain a high value of hardness (Thuillier et al., 2010). The gap between the die and the blank-holder was held fixed in both stages by means of a pile of adjustable washers put in-between. The total height of these washers was determined experimentally as large as possible in order to draw a cylindrical cup without wrinkles. For the studied material, the measured gap values are 1.0 mm for the first stage and 1.4 mm for the second stage (Thuillier et al., 2002). The blank is lubricated on both sides at the beginning of the process, as well as before the second forming stage, reducing the friction forces arising between the blank and the forming tools. The depth of the cylindrical cups is 50 mm in the first stage and 70 mm in the second stage.

Table 3
Main dimensions of the forming tools for both stages (mm) (Gelin and Picart, 1999).

Tool geometry	Stage 1	Stage 2
Die opening diameter	104.5	78.0
Die radius	8.0	5.5
Die height	21.0	16.0
Punch diameter	100.0	73.4
Punch radius	5.5	8.5
Blank-holder opening diameter	104.5	105.0
Blank-holder radius	–	7.0
Blank-holder height	10.0	30.0

The punch speed during the forming operation (both stages) is 3.3 mm/s. The accuracy reached in the measurement of the punch displacement is ± 0.02 mm, while the load is recorded with 0.4% of accuracy (Thuillier et al., 2010). Five forming tests under identical process conditions were performed in order to check the reproducibility of the obtained experimental data. After the first stage, some cylindrical cups are extracted for thickness measurement, while others are deformed in the reverse direction. The thickness of the cup wall is measured using a three-dimensional coordinate measuring machine (DEA Swift A001). Three straight lines are marked on the sheet before forming (0°, 45° and 90°) to perform the thickness measurement in three directions to the rolling direction, using an increment of 1 mm between consecutive points. Furthermore, a hole is trimmed in the bottom of the cup to fix it on the table of the measuring machine. The point coordinates are evaluated on both sides of the cylindrical cups (inside and outside) at the same height, allowing the definition of a horizontal distance measured in the radial direction (Thuillier et al., 2010), as shown in Fig. 6.

4.2. Finite element model

The numerical simulations were carried out with the in-house static implicit finite element code DD3IMP (Menezes and Teodosiu, 2000), specifically developed to simulate sheet metal forming processes (Oliveira et al., 2008). In order to improve the computational performance, some high-performance computing techniques have been incorporated to take advantage of multi-core processors, namely OpenMP directives in the most time-consuming branches of the code (Menezes et al., 2011). All numerical simulations were performed on a computer machine equipped with an Intel® Core™ i7–4770 K Quad-Core processor (3.5 GHz) and the Windows 7 Professional (64-bit platform) operating system.

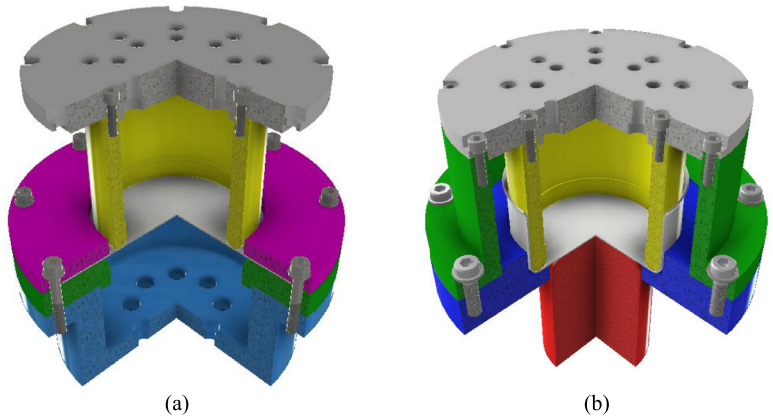

Fig. 5. Schemes of the forming tools used in the reverse deep drawing of a cylindrical cup: (a) first stage; (b) second stage.

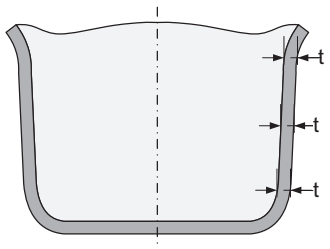

Fig. 6. Measurement of the wall thickness in the cylindrical cup.

Table 4
Number of Nagata patches used to describe each rigid forming tool involved in the reverse deep drawing process.

Tool	Stage 1	Stage 2
Die	180	260
Punch	260	210
Blank-holder	80	180
Total	520	650

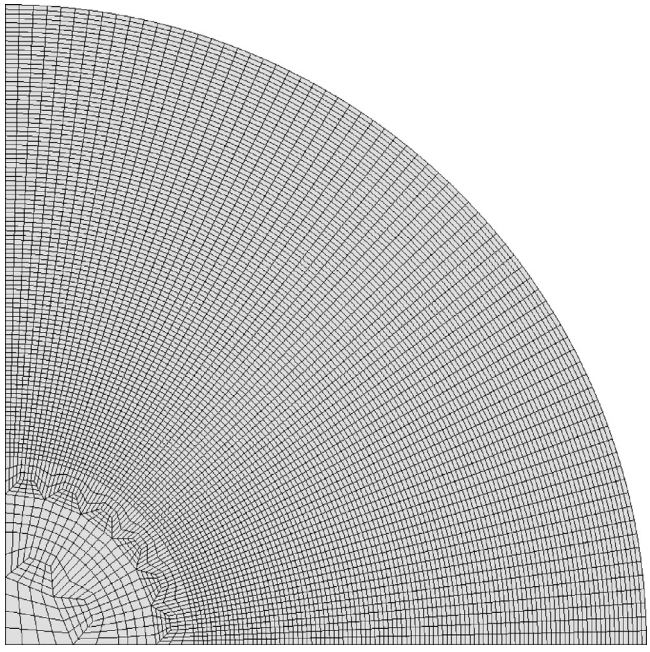

Fig. 7. Discretization of the blank using 15,408 solid finite elements (2 layers through the thickness).

4.2.1. Blank modelling

Due to geometric and material symmetry conditions, only one-quarter of the blank is modelled, which is discretized with 8-node hexahedral finite elements, associated with a selective reduced integration technique (Hughes, 1980). Using solid elements to model the blank it is possible to evaluate accurately the gradients over the thickness, as well as the contact forces (Menezes and Teodosiu, 2000; Teodosiu et al., 1995). The total number of elements is 15,408 (see Fig. 7), using 2 layers of elements through the thickness. The friction between the blank and the forming tool is modelled through the classical Coulomb's law. The value of the friction coefficient suggested in the benchmark specifications is $\mu = 0.15$, which is in accordance with the value measured by Trzepieciński et al. (2015), using three different tribological tests: strip drawing test, draw bead test and pin-on-disc tribometer, considering lubrication conditions and steady-state regions.

4.2.2. Rigid tools

Currently, the modelling of the forming tools is carried out with rigid surfaces, neglecting their elastic deformation. Thus, only the outer surface of the forming tools is modelled, which is directly used in the definition of the frictional contact constraints. In the present study, the surface of the tools is described with Nagata patches (Neto et al., 2014b, 2013), providing an accurate geometrical description (Neto et al., 2015a). The discretization of the tools involved in the reverse deep drawing process (one-quarter due to symmetry conditions) is presented in Fig. 8, for both forming stages. In order to obtain a negligible shape error, each circular arc is described by 4 Nagata patches in the radial direction while each tool is discretized with 20 patches in the circumferential direction (see Fig. 8). The total number of Nagata patches composing each forming tool for both stages is presented in Table 4. The clearance between the die and the blank-holder used in the numerical model is 1.10 mm in the first stage and 1.4 mm in the second stage. Note that the clearance adopted in the numerical model for the first forming stage is slightly larger than the experimental value (see Section 4.1).

The cup rim resulting from the first forming stage need to pass between the die and the blank-holder during the second stage, as shown in Fig. 5(b). Therefore, in order to avoid the convergence problems related to the contact between the cup rim and the sharp edge of the blank-holder, a fillet radius of 1.0 mm is introduced in the free boundary of the vertical wall, as shown in Fig. 8(b). This strategy overcomes the *flip–flop* effect arising from the contact constraints enforcement, i.e. constant switching between con-

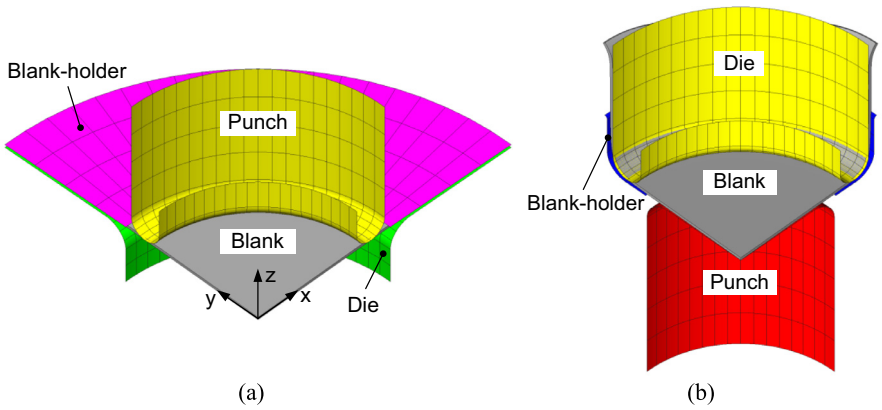

Fig. 8. Discretization of the (rigid) forming tools using Nagata patches: (a) first stage; (b) second stage.

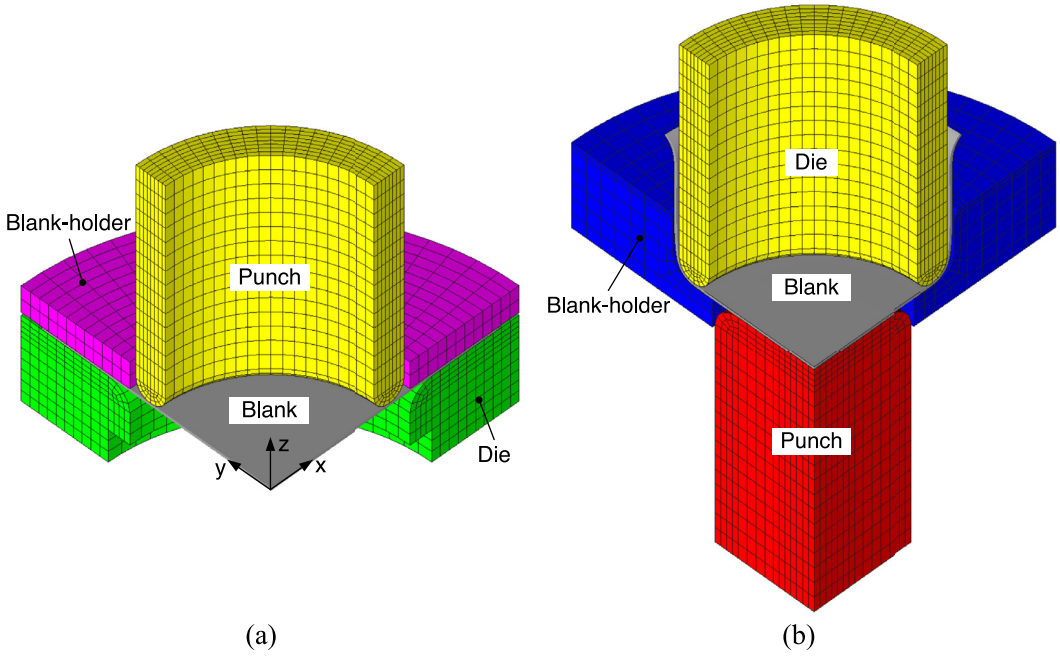

Fig. 9. Discretization of the (deformable) forming tools using solid finite elements: (a) first stage; (b) second stage.

tact and gap statuses (Neto et al., 2015). An identical procedure is adopted in the model that considers deformable tools.

4.2.3. Deformable tools

Due to geometric and material symmetry conditions, only one-quarter of the forming tools is modelled. They are discretized with solid finite elements, allowing take into account its elastic deformation. Typically, the surface details involved in the tools require a fine mesh in these zones, leading to a significant increase in the total number of finite elements. This issue can be overcome by applying a surface smoothing method on the coarse mesh, providing an accurate description of the curved surfaces using a small amount of finite elements. Several surface smoothing procedures have been proposed in the last decade (Neto et al., 2015). In the present study, each tool surface is smoothed with Nagata patches, following the procedure proposed by Neto et al. (2016) for frictional contact problems between deformable bodies.

The discretization of each forming tool involved in the reverse deep drawing process is presented in Fig. 9. The discretization of the deformable tools in the curved surfaces is identical to the previously used for rigid tools (compare Fig. 8 and Fig. 9), providing a similar shape error resulting from the surface interpolation with Nagata patches. Consequently, the geometrical accuracy of the tool surfaces is the same for both finite element models. The number of finite elements used to define each deformable forming tool is presented in Table 5. The geometry of the tools was simplified in the region of the screws (see Fig. 5), where adequate boundary conditions are applied to represent the physical connection between the die and the blank-holder. Since the screws are located on a diameter of 185 mm (see Section 4.1), the tools are modelled only within this perimeter, which is fixed in all directions, establishing an initial clearance of 1.0 mm between them. Besides, the vertical

Table 5
Number of finite elements used to describe each deformable forming tool involved in the reverse deep drawing process.

Tool	Stage 1	Stage 2
Die	2480	2880
Punch	2880	3003
Blank-holder	480	1320
Total	5840	7203

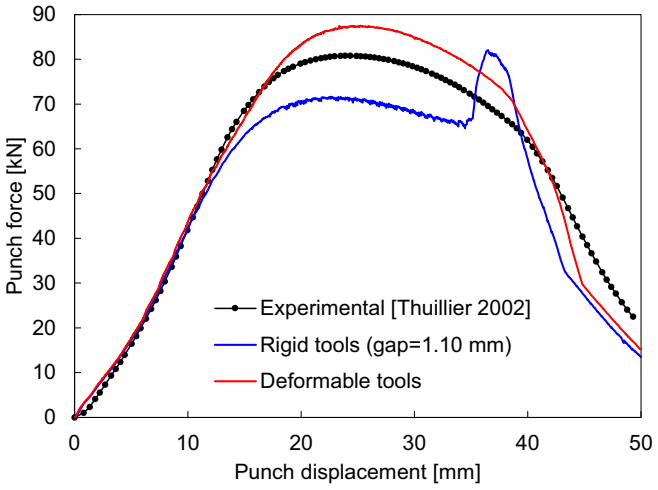

Fig. 10. Comparison between experimental and numerical punch force evolution during the first forming stage.

displacement imposed to the punch is applied on its top surface. Accordingly, an identical procedure is adopted for the tools of the second stage.

The mechanical behaviour of the forming tools is assumed elastic and isotropic (von Mises). Since the tools are made of steel, their elastic properties are identical to the ones adopted for the blank, i.e. Young's modulus of 210 GPa and Poisson ratio of 0.30. Nevertheless, their yield strength is significantly higher, about 400 MPa.

4.3. Results and discussion

The comparison between different numerical approaches to model the forming tools is presented. Furthermore, the numerical results are compared with the experimental ones provided by Thuillier et al. (2002), highlighting the influence of the tools modelling in the accuracy of the finite element solution.

4.3.1. Forming forces

The comparison between experimental and numerical punch force evolution is shown in Fig. 10, for the first forming stage. Globally, the experimental punch force is overestimated by the numerical model that takes into account the elastic deformation of the tools, while it is underestimated when considering rigid tools in the finite element model. Nevertheless, note that the clearance between the die and the blank-holder adopted in the finite element model using rigid tools (1.10 mm) is higher than the experimental value (1.0 mm). Since the deformation mode of the sheet is close to uniaxial compression in the flange (Neto et al., 2014a), the increase of the sheet thickness in this region leads to an increase of punch force due to the large restraining forces. Therefore, the clearance between the die and the blank-holder was enlarged to avoid the ironing of the flange in the finite element simulation. However, the adopted value of clearance (1.10 mm) is not sufficient to completely eliminate the ironing effect, which is highlighted by the abrupt increase of the punch force at approximately 35 mm of punch displacement (see Fig. 10). On the other hand, the punch force evolution provided by the numerical model using deformable tools (1.0 mm of initial gap) is in better agreement with the experimental one, as shown in Fig. 10. The sudden decrease of the punch force at around 43 mm of displacement occurs for both numerical models (rigid and deformable tools), which is related to the loss of contact between the sheet and the blank-holder. The possible misalignment of the sheet with the forming tools in the experimental procedure may explain the smoother decrease of the experimental punch force.

Although the mesh adopted in the discretization of the deformable forming tools (Fig. 9) can be considered coarse, the evolution of the punch force is smooth (see Fig. 10). This is related with the applied surface smoothing procedure (Neto et al., 2016), which eliminates the nonphysical oscillations in the contact force induced by the discontinuity of the surface normal vector field. The nodal contact forces arising in the slave nodes belonging to the symmetry plane are presented in Fig. 11, for the instant corresponding to 25 mm of punch displacement. The contact occurs mainly in the curved zones of the forming tools, where it is possible to see that the surface smoothing method is effective. In fact, the contact forces are properly distributed on the smoothed surface, despite the apparent gap between the punch and the sheet (see Fig. 11(a)) and between the die and the sheet (see Fig. 11(b)), in the curved contact zones.

Concerning the second forming stage, Fig. 12 presents the comparison between experimental and numerical punch force evolution. The numerical results are similar for both finite element models (rigid and deformable tools), indicating that the tools deformation is negligible in the second stage. The numerical punch force evolution is in very good agreement with the experimental one during the initial 35 mm of punch displacement. In fact, the initial slope predicted by the numerical simulation is coincident with the experimental one. On the other hand, the experimental punch force exhibits a peak for a punch stroke around 40 mm, which is underestimated by the numerical simulation, both in terms of value and the instant of occurrence, as shown in Fig. 12. Since the cylindrical cup is not completely formed, this peak of the force is associated with the passage of the cup rim between the die and the blank-holder (see Fig. 9(b)). The difference between numerical and experimental force peak is connected with the final value of the punch force in the first forming stage (see Fig. 10), which is underestimated by the numerical simulation. Thus, the slight misalignment of the sheet with the forming tools in the experimental setup can lead to an increase of the restraining forces arising in the cup rim.

The evolution of the blank-holder force as a function of the punch displacement is presented in Fig. 13, for both forming stages, comparing the two numerical models developed. Regarding the first stage, the force value predicted by the model that takes into account the tools deformation is globally higher than the one obtained considering rigid tools. Note that the fixed clearance between the die and the blank-holder is larger in the finite element model using rigid tools (1.10 mm). The abrupt increase of the blank-holder force at approximately 35 mm of punch displacement (see Fig. 13) is a consequence of the ironing effect in the flange, which only occurs when using rigid tools in the finite element model. The magnitude of the blank-holder force during the second forming stage is considerably lower than in the first stage, as shown in Fig. 13, since the clearance between the die and the blank-holder is larger (see Section 2). Moreover, the small difference between the two finite element models in terms of predicted forces indicates an insignificant deflection of the tools in the second stage.

4.3.2. Tools deflection

The deflection of the tools during the first forming stage is assessed in the present study through the nodal displacements evaluated in the tools, specifically the blank-holder and the die. Fig. 14 presents the evolution of the vertical displacement of six nodes (three positioned in the blank-holder and three in the die) as a function of the punch displacement. The deformation of the tools comes up from the thickening of the flange, which is induced by the circumferential compressive stress state (uniaxial compressive

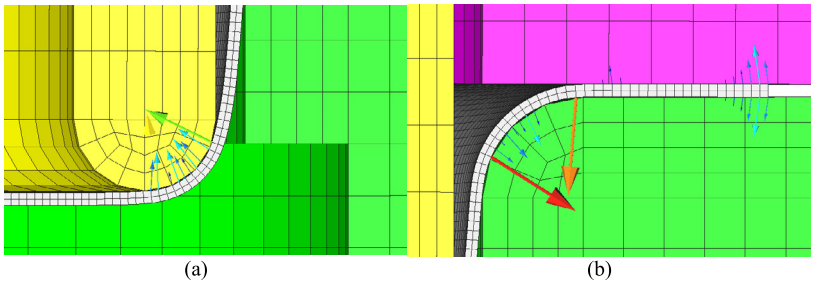

Fig. 11. Nodal contact forces in the slave nodes for 25 mm of punch displacement (magnitude denoted by arrow size and colour): (a) contact between sheet and punch; (b) contact between sheet and die as well as between sheet and blank-holder.

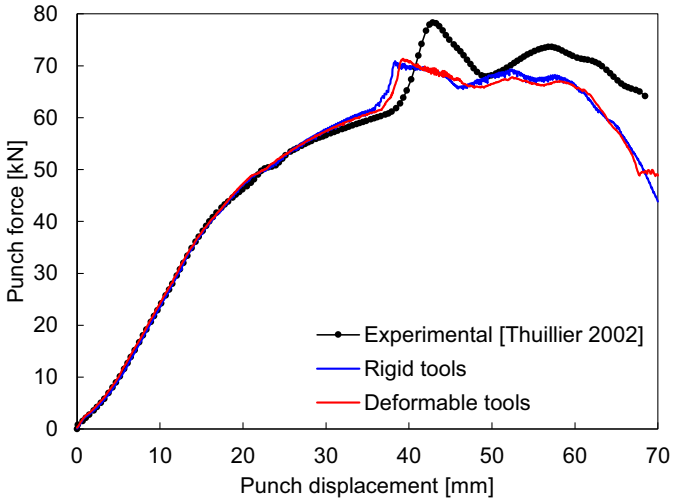

Fig. 12. Comparison between experimental and numerical punch force evolution during the second forming stage.

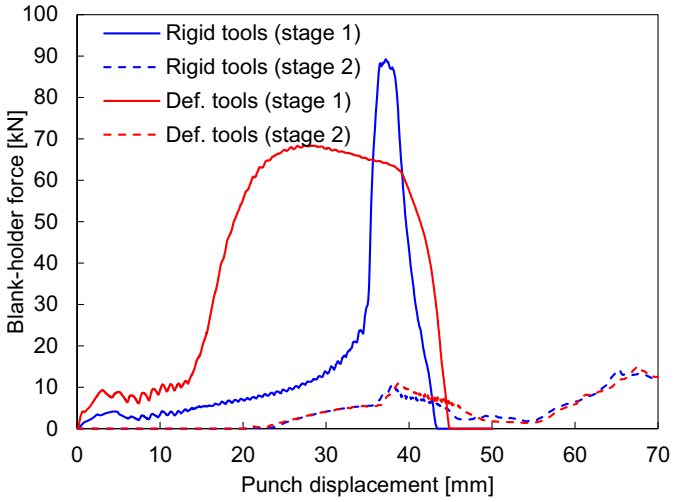

Fig. 13. Evolution of the predicted blank-holder force as a function of the punch displacement for both forming stages, comparing rigid and deformable forming tools.

strain). In order to quantify the influence of the plastic anisotropy of the sheet (see Fig. 2) in the elastic deformation of the forming tools, the selected nodes are positioned along the circumferential direction, namely in the rolling direction (RD), diagonal direction (DD) and transverse direction (TD). The nodes 1, 2 and 3 are located in the open diameter of the blank-holder (contact surface), while the nodes 4, 5 and 6 are located in the die radius

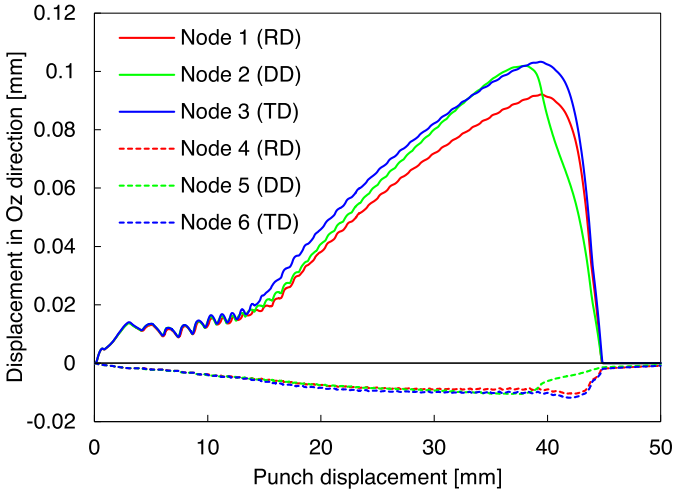

Fig. 14. Vertical displacement of three nodes (node 1, 2 and 3) located in the open diameter of the blank-holder and three nodes (node 4, 5 and 6) located in the die radius (first forming stage).

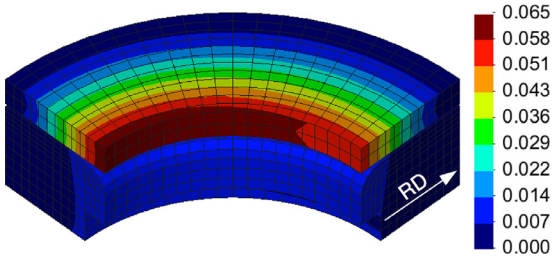

Fig. 15. Contour plot of the nodal displacements (mm) in the die and blank-holder for 25 mm of punch displacement.

(transition with horizontal contact surface). Adopting the finite element model with deformable tools, the effective clearance between the die and the blank-holder increases gradually and then drops quickly to the initial value when the sheet loses contact with the blank-holder, as shown in Fig. 14. The maximum value of clearance achieved (about 1.11 mm) occurs for 40 mm of punch displacement, which is the instant where ironing of the flange occurs using rigid tools (see Fig. 10). Hence, the clearance of 1.10 mm adopted in the model with rigid tools is insufficient to accommodate the increase in thickness. Since the die is roughly 3 times thicker than the blank-holder (Fig. 9(a)), the nodal vertical displacements are significantly larger in the blank-holder, as highlighted in Fig. 14.

The contour plot of the nodal displacements in the die and blank-holder is presented in Fig. 15, for the instant corresponding to 25 mm of punch displacement. Due to the boundary conditions applied in the outer perimeter of the die and blank-holder, the nodal displacements are zero in this region. The largest value of

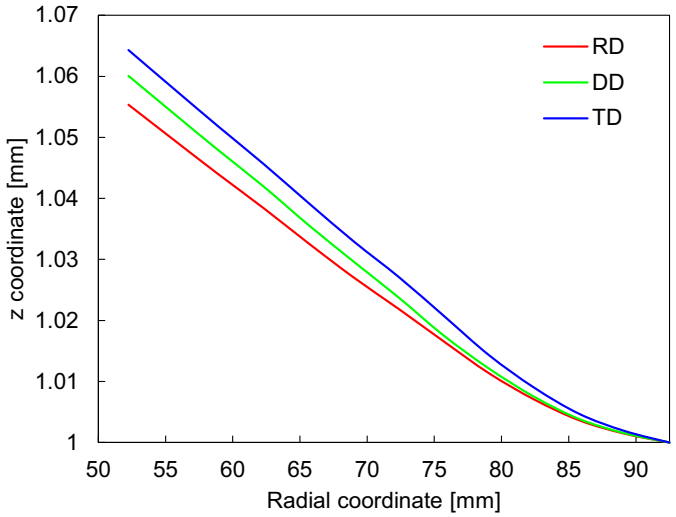

Fig. 16. Profile of the blank-holder surface (first forming stage) measured in three directions, for 25 mm of punch displacement.

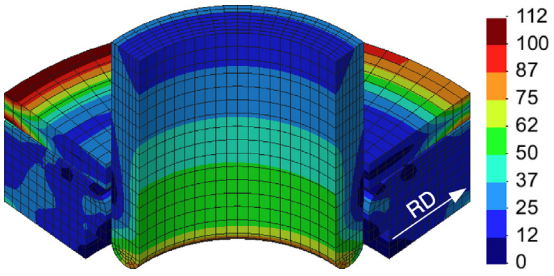

Fig. 17. von Mises stress distribution (MPa) in the forming tools for 25 mm of punch displacement.

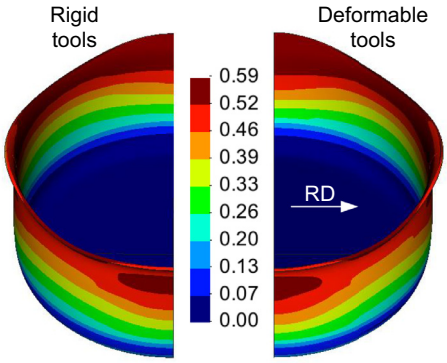

Fig. 18. Equivalent plastic strain distribution plotted in the deformed configuration of the cylindrical cup after the first forming stage. Finite element model using rigid tools (left) and using deformable tools (right).

Fig. 19. Experimental geometry of the cylindrical cup obtained by reverse deep drawing: (a) first stage; (b) second stage.

displacement occurs in the blank-holder opening diameter, which is predominantly in the vertical direction. On the other hand, for the same radial distance, the deflection of the die is at least 5 times lower than the one of blank-holder. Indeed, the maximum value of the nodal displacements is inferior to 0.014 mm in the die (see Fig. 15).

The deformed configuration of the blank-holder involved in the first forming stage is presented in Fig. 16, for the instant corresponding to 25 mm of punch displacement. In order to analyse the influence of the sheet anisotropy in the blank-holder deflection, three different cross sections are assessed, namely in the RD, DD and TD. The profile of the deformed blank-holder is different for each analysed cross section (see Fig. 16), because the predicted thickness distribution is non-uniform in the circumferential direction and the draw-in is asymmetric. Indeed, the thickness of the flange and its draw-in are directly connected through the assumption of the incompressibility condition (Neto et al., 2014a), presenting opposite effects on the blank-holder deflection. Accordingly, the clearance between the die and the blank-holder is larger in the TD and smaller in the RD, as shown in Fig. 16. However, the relative trend between the three sections presents changes during the forming process evolution, specifically in the DD (see Fig. 14).

The von Mises stress distribution in the forming tools (punch, blank-holder and die) is presented in Fig. 17, for the instant corresponding to 25 mm of punch displacement. The maximum value of the stress arises close to the perimeter of the blank-holder due to the applied boundary conditions (prescribed displacements) and small stiffness of the blank-holder in comparison with the die. Since the maximum value of equivalent stress predicted by the numerical simulation is about 112 MPa, the forming tools only exhibit elastic deformation during the cup forming. Additionally, the stress distribution is asymmetric in the tools (Fig. 17), which is induced by the plastic anisotropy of the sheet. Nevertheless, the stress distribution in the punch is less influenced by the plastic anisotropy of the sheet, since the contact zone is almost insensitive to sheet thickness variations.

4.3.3. Cup geometry

The significant deflection of the blank-holder during the first forming stage affects the material flow, as the distribution of contact pressure on the flange is different from the one obtained using rigid tools (Shulkin et al., 1996). The equivalent plastic strain distribution predicted by finite element simulation is presented in Fig. 18, at the end of the first forming stage, comparing the numerical models analysed (rigid and deformable tools). Although the elastic deformation of the blank-holder is non-negligible (Fig. 15), the final configuration of the cylindrical cup is identical for both numerical models. Since the punch force is nonzero at the end of the first stage (see Fig. 10), the cup is not fully drawn, as shown in the experimental geometry of the cup after the first stage presented in Fig. 19(a). The maximum value of plastic strain predicted by the numerical model is reached in the cup rim. The value of equivalent plastic strain is lower in the DD for the same cup height, which is in accordance with the earing profile (four ears).

The final configuration of the cylindrical cup after the second forming stage is presented in Fig. 20, comparing the two finite element models proposed in Section 3. The main difference occurs in the DD, where the numerical model that takes into account the elastic deformation of the forming tools predicts the occurrence of wrinkling. The large circumferential compressive stress and the earing effect induced by the plastic anisotropy yields the

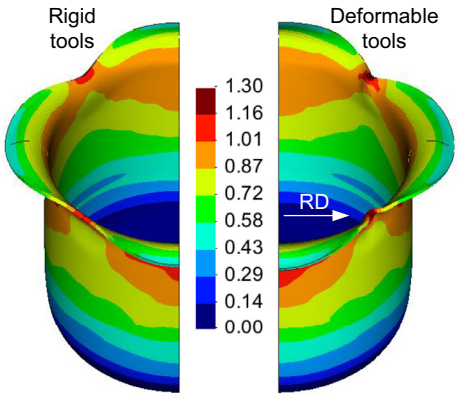

Fig. 20. Equivalent plastic strain distribution plotted in the deformed configuration of the cylindrical cup after the second forming stage. Finite element model using rigid tools (left) and using deformable tools (right).

wrinkling defect, when the flange loses contact with the blank-holder. In fact, the amplitude of the ears at the end of the first forming stage is larger when considering the elastic deformation of the forming tools, because the effective clearance between the die and the blank-holder is smaller and, consequently, the restraining forces are higher (see Fig. 13). The equivalent plastic strain distribution predicted by numerical simulation is shown in Fig. 20, comparing both numerical models. The maximum value occurs in the cup rim, specifically in the region of wrinkling. The predicted plastic strain distribution is similar for both numerical models, except in the wrinkling region. Since the plastic strain increases in the second forming stage, the amplitude of the four ears is enlarged from the first to the second drawing stage (compare Fig. 18 with Fig. 20), which is in accordance with the experimental observations (see Fig. 19). The slight misalignment of the sheet with the forming tools in the experimental procedure is confirmed by the asymmetry in the rim of the cylindrical cup, shown in Fig. 19(b).

4.3.4. Thickness distribution

The comparison between experimental and numerical thickness distribution in the cup wall after the first forming stage is shown in Fig. 21, for three different directions (RD, DD and TD). The numerical thickness is evaluated in the radial direction (see Fig. 6) according to the experimental procedure. Globally, the thickness distribution predicted by the numerical model that takes into account the elastic deformation of the forming tools is in very good agreement with the experimental evolution, as shown in Fig. 21. On the other hand, the cup thickness is clearly overestimated when the forming tools are assumed as rigid.

Since the effective clearance between the die and the blank-holder is lower when the deformation of the forming tools is taken into account (model with rigid tools presents a fixed value of 1.10 mm), the restraining forces arising in the flange are globally higher (see Fig. 13). Thus, the predicted cup wall thickness is lower and the height of the cylindrical cup is slightly higher using the finite element model with deformable tools. This difference in the cup height delays the instant in which the punch force increases abruptly during the second forming stage (see Fig. 12), which is associated with the passage of the cup rim between the die and the blank-holder. Due to the plastic anisotropy of the sheet (Fig. 2), the cup wall is thicker in the DD (see Fig. 21), which is in accordance with the earing profile presented in Fig. 18. The assumption of rigid tools leads to an unexpected decrease of the predicted thickness in the TD for 28 mm of cup height (see Fig. 21(c)), which is associated with the flange ironing, i.e. the abrupt increase of the blank-holder force shown in Fig. 13. The ironing effect occurs mainly in this direction since the anisotropic behaviour yields a sheet thickening higher in TD, as highlighted in the blank-holder deflection shown in Fig. 16.

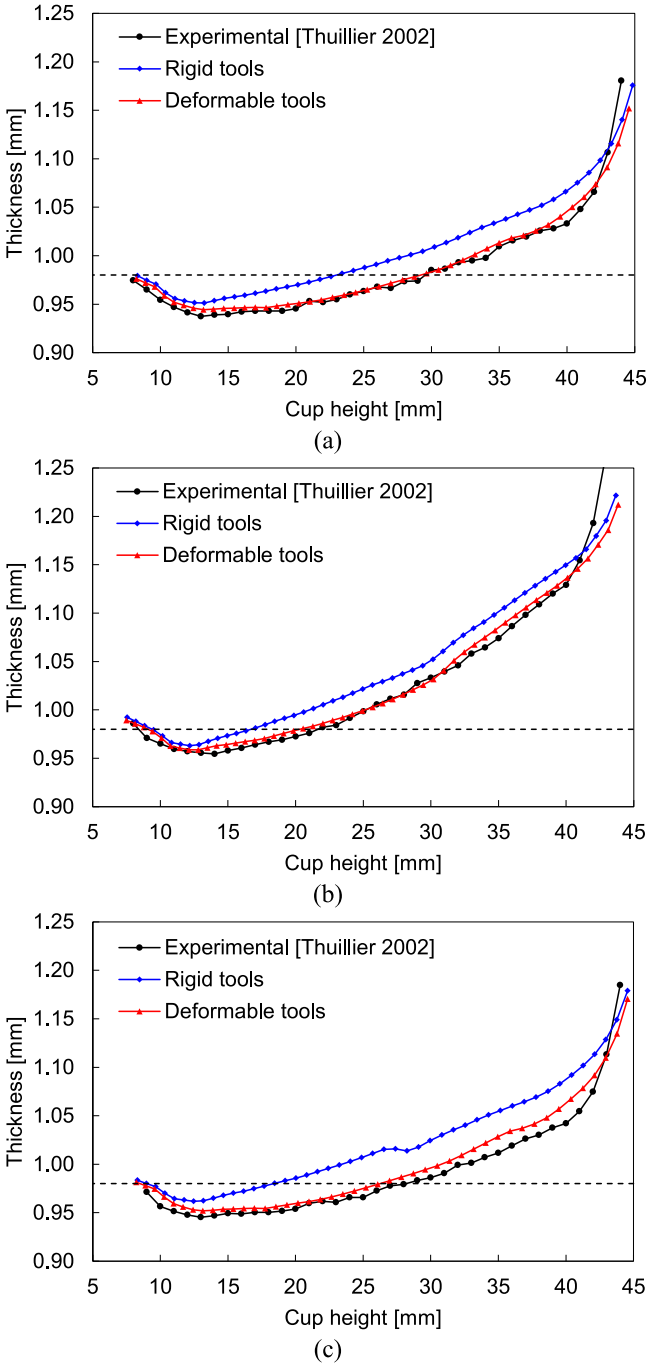

Fig. 21. Experimental and numerical thickness distributions in the cup wall after the first forming stage at: (a) RD; (b) DD; (c) TD.

The comparison between experimental and numerical thickness distribution in the cup wall after the second forming stage is presented in Fig. 22, for three different directions (RD, DD and TD). The experimental thickness distribution is overestimated in all directions by both numerical models. Nevertheless, the accuracy of the finite element model that takes into account the deformation of the forming tools is better than the one assuming rigid tools. This improvement results mainly from the numerical thickness distribution achieved for the first forming stage (see Fig. 21), which is in very good agreement with the experimental measurement,

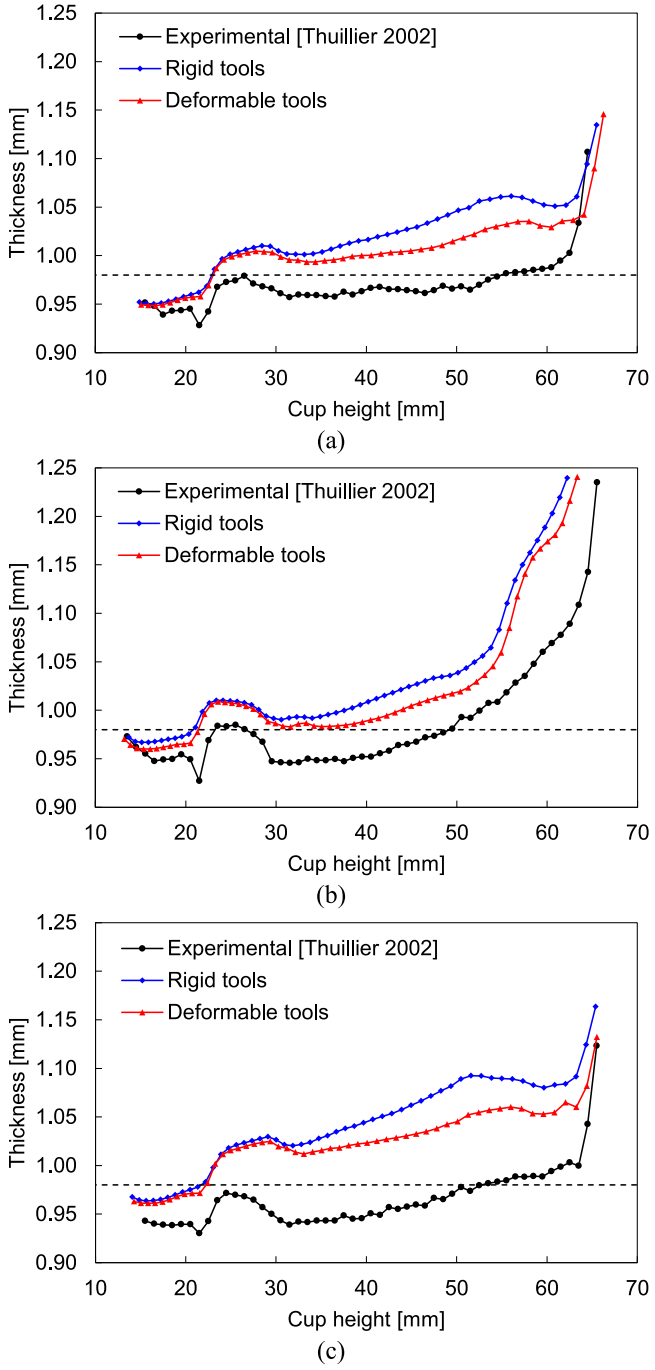

Fig. 22. Experimental and numerical thickness distributions in the cup wall after the second forming stage at: (a) RD; (b) DD; (c) TD.

when the tools deformation is considered. Indeed, the slope of the thickness distribution predicted by the numerical model with deformable tools is in good agreement with the experimental one, specifically in the RD and TD. On the other hand, this finite element model predicts the occurrence of wrinkling in the DD (see Fig. 20), which overestimate considerably the wall thickness for a cup height superior to 55 mm, as shown in Fig. 22(b).

The thickness predicted by finite element simulation is higher than the one measured experimentally because the value of the restraining forces arising in the cup rim during the second forming stage (40 mm of punch displacement) is underestimated, as shown in Fig. 12. Since the thickness of the cup wall is overestimated by the finite element simulation (Fig. 22), the cup height is underestimated. Consequently, for the same punch displacement, the small length of the flange located between the die and the blank-holder induces a delay of the punch force evolution after its peak, as highlighted in Fig. 12.

Table 6
Computational performance of both finite element models used in the reverse deep drawing simulation.

	Stage 1		Stage 2	
	Rigid tools	Deformable tools	Rigid tools	Deformable tools
Nº increments	928	2641	761	1637
Average nº iterations	6.65	7.50	6.95	8.58
Computational time [h]	1.37	18.88	1.13	10.48

4.3.5. Computational performance

The computational performance of the proposed finite element models is presented in Table 6. The adoption of the numerical model that takes into account the elastic deformation of the forming tools leads to an increase in the number of increments, the average number of iterations and the computational time. Although the significant improvements achieved in the accuracy of the numerical results (punch force evolution and thickness distribution), the computational cost increases considerably, as shown in Table 6.

Regarding the first forming stage, the computational time increases roughly 14 times in comparison with the model that uses rigid tools, while it increases approximately 9 times in the second stage. Indeed, the increase of the computational cost is a consequence of several factors: (i) higher number of DOF due to the discretization of the tools with solid elements (see Table 5); (ii) update the nonzero pattern of the global tangent matrix in each increment due to large sliding (Neto et al., 2016); (iii) small increment size required to avoid convergence problems and (iv) higher number of iterations per increment. Since the contact between a deformable body and a rigid surface is a particular case of the contact between two deformable bodies, the number of increments required in each forming stage increases when the forming tools are assumed deformable. In fact, the number of increments is approximately 3 times higher in the first stage and about 2 times in the second forming stage.

5. Conclusions

The elastic deformation of the forming tools during the reverse deep drawing of a cylindrical cup is evaluated in the present paper. The blank-holder and the die are connected by means of screws and adjustable washers put in-between, establishing a fixed initial clearance between them. Two distinct finite element models are developed to quantify the influence of the tools deformation on the material flow, i.e. the forming tools are assumed perfectly rigid as well as deformable. Moreover, the obtained numerical results are compared with the experimental measurements to validate the proposed finite element model.

The distribution of the contact pressure in the flange and, consequently, the material flow are strongly influenced by the assumptions adopted in the numerical model concerning the forming tools. The elastic deflection of the blank-holder is a consequence of the sheet thickening, which is induced by the circumferential compressive stress arising in the flange. Therefore, taking into account the deformation of the tools in the numerical model, the effective clearance between the die and the blank-holder increases during the forming process, while the restraining forces in the flange are lower. Indeed, the predicted clearance increases about 10% during the first forming stage, while the deflection of the tools is negligi-

ble in the second stage. Accordingly, the experimental punch force of the first forming stage is slightly overestimated by this numerical model, while the assumption of rigid tools leads to the ironing effect in the flange. Besides, considering the elastic deformation of the forming tools, the predicted thickness distribution in the cup wall is in very good agreement with the experimental measurements. Nevertheless, the computational cost is significantly higher in comparison with the classic model using rigid tools.

Therefore, the accuracy of the sheet metal forming simulation can be improved considering the elastic deformation of the forming tools in the numerical model. This is particularly important in forming processes of high strength steels and reduced structural stiffness of the tools, where the deflection of the tools is substantial. However, the computational time increases considerably in comparison with the assumption of rigid tools. Thus, the numerical model that takes into account the elastic deformation of the forming tools should be adopted only in specific cases.

Acknowledgements

The authors gratefully acknowledge the financial support of the Portuguese Foundation for Science and Technology (FCT) under projects with reference UID/EMS/00285/2013, P2020-PTDC/EMS-TEC/0702/2014 (POCI-01-0145-FEDER-016779) and P2020-PTDC/EMS-TEC/6400/2014 (POCI-01-0145-FEDER-016876) by UE/FEDER through the program COMPETE2020. The first author is also grateful to the FCT for the Postdoctoral grant SFRH/BPD/101334/2014.

References

Alart, P., Curnier, A., 1991. A mixed formulation for frictional contact problems prone to Newton like solution methods. Comput. Methods Appl. Mech. Eng. 92, 353–375. doi:10.1016/0045-7825(91)90022-X.

Alart, P.P., 1997. Méthode de Newton généralisée en mécanique du contact. J. Math. Pures Appl. 76, 83–108. doi:10.1016/S0021-7824(97)89946-1.

Alves, J.L., 2003. Simulação Numérica do Processo de Estampagem de Chapas Metálicas: Modelação Mecânica e Métodos Numéricos. University of Minho.

Alves, J.L., Bouvier, S., Jomaâ, M., Billardon, R., Oliveira, M.C., Menezes, L.F., 2007. Kinematic hardening: characterization, modeling and impact on springback prediction. AIP Conf. Proc. 908, 691–698. doi:10.1063/1.2740891.

Belytschko, T., Liu, W.K., Moran, B., 2000. Nonlinear Finite Elements for Continua and Structures. John Wiley & Sons.

Cavalieri, F.J., Cardona, A., 2015. Numerical solution of frictional contact problems based on a mortar algorithm with an augmented Lagrangian technique. Multibody Syst. Dyn. doi:10.1007/s11044-015-9449-8.

Chalal, H., Racz, S.-G., Balan, T., 2012. Springback of thick sheet AHSS subject to bending under tension. Int. J. Mech. Sci. 59, 104–114. doi:10.1016/j.ijmecsci.2012.03.011.

Chen, J., Xu, D., Xia, G., Li, X., Chen, J., Zhang, J., Yan, W., Li, Y., 2012. Geometric compensation for automotive stamping die design integrating structure deflection and blank thinning. Int. J. Adv. Manuf. Technol. 66, 1449–1456. doi:10.1007/s00170-012-4422-7.

Chen, K., Scales, M., Kyriakides, S., Corona, E., 2016. Effects of anisotropy on material hardening and burst in the bulge test. Int. J. Solids Struct. 82, 70–84. doi:10.1016/j.ijsolstr.2015.12.012.

Chenot, J.-L., Bernacki, M., Bouchard, P.-O., Fourment, L., Hachem, E., Perchat, E., 2014. Recent and future developments in finite element metal forming simulation. 11th Int. Conf. Technol. Plast. ICTP 2014.

Choi, K.Y., Lee, M.G., Kim, H.Y., 2013. Sheet metal forming simulation considering die deformation. Int. J. Automot. Technol. 14, 935–940. doi:10.1007/s12239-013-0103-2.

Chun, B.K., Kim, H.Y., Lee, J.K., 2002. Modeling the Bauschinger effect for sheet metals, part II: applications. Int. J. Plast. 18, 597–616. doi:10.1016/S0749-6419(01)00047-X.

Dafalias, Y.F., 1985. The Plastic Spin. J. Appl. Mech. 52, 865–871. doi:10.1115/1.3169160.

Dasappa, P., Inal, K., Mishra, R., 2012. The effects of anisotropic yield functions and their material parameters on prediction of forming limit diagrams. Int. J. Solids Struct. 49, 3528–3550. doi:10.1016/j.ijsolstr.2012.04.021.

Del Pozo, D., López de Lacalle, L.N., López, J.M., Hernández, A., 2007. Prediction of press/die deformation for an accurate manufacturing of drawing dies. Int. J. Adv. Manuf. Technol. 37, 649–656. doi:10.1007/s00170-007-1012-1.

Diller, M., Thomas, W., Ahmetoglu, M.A., Akgerman, N., Altan, T., 1997. Applications of computer simulations for part and process design for automotive stampings SAE Technical Paper 970985. doi:10.4271/970985.

Doege, E., Elend, L.-E., 2001. Design and application of pliable blank holder systems for the optimization of process conditions in sheet metal forming. J. Mater. Process. Technol. 111, 182–187. doi:10.1016/S0924-0136(01)00506-4.

Frederick, C.O., Armstrong, P.J., 2007. A mathematical representation of the multiaxial Bauschinger effect. Mater. High Temp. 24, 1–26. doi:10.1179/096034007X207589.

Gelin, J.C., Picart, P., 1999. NUMISHEET'99 Benchmark. In: Proceedings of the 4th International Conference on Numerical Simulation of 3D Sheet Forming Processes. Besançon.

Ghaei, A., 2012. Numerical simulation of springback using an extended return mapping algorithm considering strain dependency of elastic modulus. Int. J. Mech. Sci. 65, 38–47. doi:10.1016/j.ijmecsci.2012.09.002.

Grilo, T.J., Vladimirov, I.N., Valente, R.A.F., Reese, S., 2016. A finite strain constitutive model for non-quadratic yield criteria and nonlinear kinematic/isotropic hardening: application to sheet metal forming. Arch. Appl. Mech. 86, 147–163. doi:10.1007/s00419-016-1117-9.

Großmann, K., Wiemer, H., Hardtmann, A., Penter, L., Kriechenbauer, S., 2009. Adjusting the contact surface of forming tools in order to compensate for elastic deformations during the process. In: Proceedings of the 7th European LS-DYNA Conference. Salzburg, Austria.

Haddadi, H., Bouvier, S., Banu, M., Maier, C., Teodosiu, C., 2006. Towards an accurate description of the anisotropic behaviour of sheet metals under large plastic deformations: modelling, numerical analysis and identification. Int. J. Plast. 22, 2226–2271. doi:10.1016/j.ijplas.2006.03.010.

Hallquist, J.O., 2007. LS-DYNA keyword user's manual. Livermore Softw. Technol. Corp. 970.

Hallquist, J.O., Goudreau, G.L., Benson, D.J., 1985. Sliding interfaces with contact-impact in large-scale Lagrangian computations. Comput. Methods Appl. Mech. Eng. 51, 107–137. doi:10.1016/0045-7825(85)90030-1.

Heegaard, J.-H., Curnier, A., 1993. An augmented Lagrangian method for discrete large-slip contact problems. Int. J. Numer. Methods Eng. 36, 569–593. doi:10.1002/nme.1620360403.

Heege, A., Alart, P., 1996. A frictional contact element for strongly curved contact problems. Int. J. Numer. Methods Eng. 39, 165–184. doi:10.1002/(SICI)1097-0207(19960115)39:1⟨165::AID-NME846⟩3.0.CO;2-Y.

Hill, R., 1948. A theory of the yielding and plastic flow of anisotropic metals. Proc. R. Soc. A Math. Phys. Eng. Sci. 193, 281–297. doi:10.1098/rspa.1948.0045.

Hoffmann, J., 2005. Berücksichtigung der Elastischen Werkzeugeigenschaften in der Blechumformsimulation. Hochschule Lausitz University of Applied Sciences.

Hughes, T.J.R., 1980. Generalization of selective integration procedures to anisotropic and nonlinear media. Int. J. Numer. Methods Eng. 15, 1413–1418. doi:10.1002/nme.1620150914.

Hughes, T.J.R., Winget, J., 1980. Finite rotation effects in numerical integration of rate constitutive equations arising in large-deformation analysis. Int. J. Numer. Methods Eng. 15, 1862–1867. doi:10.1002/nme.1620151210.

Keum, Y.T., Ahn, I.H., Lee, I.K., Song, M.H., Kwon, S.O., Park, J.S., 2005. Simulation of stamping process of automotive panel considering die deformation. AIP Conf. Proc. 778, 90–95. doi:10.1063/1.2011199.

Konyukhov, A., Schweizerhof, K., 2008. On the solvability of closest point projection procedures in contact analysis: Analysis and solution strategy for surfaces of arbitrary geometry. Comput. Methods Appl. Mech. Eng. 197, 3045–3056. doi:10.1016/j.cma.2008.02.009.

Laursen, T.A., Simo, J.C., 1993. A continuum-based finite element formulation for the implicit solution of multibody, large deformation-frictional contact problems. Int. J. Numer. Methods Eng. 36, 3451–3485. doi:10.1002/nme.1620362005.

Lee, J., Ha, J., Bong, H.J., Kim, D., Lee, M.-G., 2016. Evolutionary anisotropy and flow stress in advanced high strength steels under loading path changes. Mater. Sci. Eng. A. doi:10.1016/j.msea.2016.06.074.

Lingbeek, R.A., Meinders, T., 2007. Towards efficient modelling of macro and micro tool deformations in sheet metal forming. AIP Conf. Proc. 908, 723–728.

Mario, H., Dietrich, W., Gfrerrer, A., Lang, J., 2013. Integrated Computer-Aided Design in Automotive Development. Springer, Berlin Heidelberg doi:10.1007/978-3-642-11940-8.

Mattiasson, K., Jergéus, J., DuBois, P., 2014. On the prediction of failure in metal sheets with special reference to strain path dependence. Int. J. Mech. Sci. 88, 175–191. doi:10.1016/j.ijmecsci.2014.08.006.

McMeeking, R.M., Rice, J.R., 1975. Finite-element formulations for problems of large elastic-plastic deformation. Int. J. Solids Struct. 11, 601–616. doi:10.1016/0020-7683(75)90033-5.

Menezes, L.F., Neto, D.M., Oliveira, M.C., Alves, J.L., 2011. Improving computational performance through HPC techniques: case study using DD3IMP in-house code. AIP Conf. Proc. 1353, 1220–1225. doi:10.1063/1.3589683.

Menezes, L.F., Teodosiu, C., 2000. Three-dimensional numerical simulation of the deep-drawing process using solid finite elements. J. Mater. Process. Technol. 97, 100–106. doi:10.1016/S0924-0136(99)00345-3.

Mijar, A.R., Arora, J.S., 2000. Study of variational inequality and equality formulations for elastostatic frictional contact problems. Arch. Comput. Methods Eng. 7, 387–449. doi:10.1007/BF02736213.

Msolli, S., Badreddine, H., Labergere, C., Martiny, M., Robin, G., Jrad, M., Saanouni, K., Choquart, F., 2015. Experimental characterization and numerical prediction of ductile damage in forming of AA1050-O sheets. Int. J. Mech. Sci. 99, 262–273. doi:10.1016/j.ijmecsci.2015.05.020.

Neto, D.M., Oliveira, M.C., Alves, J.L., Menezes, L.F., 2014a. Influence of the plastic anisotropy modelling in the reverse deep drawing process simulation. Mater. Des. 60, 368–379. doi:10.1016/j.matdes.2014.04.008.

Neto, D.M., Oliveira, M.C., Alves, J.L., Menezes, L.F., 2015a. Comparing faceted and smoothed tool surface descriptions in sheet metal forming simulation. Int. J. Mater. Form. 8, 549–565. doi:10.1007/s12289-014-1177-8.

Neto, D.M., Oliveira, M.C., Dick, R.E., Barros, P.D., Alves, J.L., Menezes, L.F., 2015b. Numerical and experimental analysis of wrinkling during the cup drawing of an AA5042 aluminium alloy. Int. J. Mater. Form doi:10.1007/s12289-015-1265-4.

Neto, D.M., Oliveira, M.C., Menezes, L.F., 2015. Surface smoothing procedures in computational contact mechanics. Arch. Comput. Methods Eng. doi:10.1007/s11831-015-9159-7.

Neto, D.M., Oliveira, M.C., Menezes, L.F., Alves, J.L., 2013. Nagata patch interpolation using surface normal vectors evaluated from the IGES file. Finite Elem. Anal. Des. 72, 35–46. doi:10.1016/j.finel.2013.03.004.

Neto, D.M., Oliveira, M.C., Menezes, L.F., Alves, J.L., 2014b. Applying Nagata patches to smooth discretized surfaces used in 3D frictional contact problems. Comput. Methods Appl. Mech. Eng. 271, 296–320. doi:10.1016/j.cma.2013.12.008.

Neto, D.M., Oliveira, M.C., Menezes, L.F., Alves, J.L., 2016. A contact smoothing method for arbitrary surface meshes using Nagata patches. Comput. Methods Appl. Mech. Eng. 299, 283–315. doi:10.1016/j.cma.2015.11.011.

OECD, 2011. Recent developments in the automobile industry, OECD Economics Department Policy Notes, No. 7.

Oliveira, M.C., Alves, J.L., Menezes, L.F., 2008. Algorithms and Strategies for Treatment of Large Deformation Frictional Contact in the Numerical Simulation of Deep Drawing Process. Arch. Comput. Methods Eng. 15, 113–162. doi:10.1007/s11831-008-9018-x.

Pietrzak, G., Curnier, A., 1999. Large deformation frictional contact mechanics: continuum formulation and augmented Lagrangian treatment. Comput. Methods Appl. Mech. Eng. 177, 351–381. doi:10.1016/S0168-874X(00)00029-9.

Prager, W., 1949. Recent Developments in the Mathematical Theory of Plasticity. J. Appl. Phys. 20, 235. doi:10.1063/1.1698348.

Shulkin, L., Jansen, S.W., Ahmetoglu, M.A., Kinzel, G.L., Altan, T., 1996. Elastic deflections of the blank holder in deep drawing of sheet metal. J. Mater. Process. Technol. 59, 34–40. doi:10.1016/0924-0136(96)02284-4.

Simo, J.C., Taylor, R.L., 1985. Consistent tangent operators for rate-independent elastoplasticity. Comput. Methods Appl. Mech. Eng. 48, 101–118. doi:10.1016/0045-7825(85)90070-2.

Struck, R., Medricky, M., Düngen, M., Kulp, S., Behrens, B.A., Krimm, R., 2008. Considering tool and press elasticity within the forming simulation and experimental validation. LS-DYNA Anwenderforum.

Taherizadeh, A., Green, D.E., Yoon, J.W., 2015. A non-associated plasticity model with anisotropic and nonlinear kinematic hardening for simulation of sheet metal forming. Int. J. Solids Struct. 69-70, 370–382. doi:10.1016/j.ijsolstr.2015.05.013.

Teodosiu, C., Daniel, D., Cao, H.-L., Duval, J.-L., 1995. Modelling and simulation of the can-making process using solid finite elements. J. Mater. Process. Technol. 50, 133–143. doi:10.1016/0924-0136(94)01375-B.

Thuillier, S., Manach, P.Y., Menezes, L.F., 2010. Occurence of strain path changes in a two-stage deep drawing process. J. Mater. Process. Technol. 210, 226–232. doi:10.1016/j.jmatprotec.2009.09.004.

Thuillier, S., Manach, P.Y., Menezes, L.F., Oliveira, M.C., 2002. Experimental and numerical study of reverse re-drawing of anisotropic sheet metals. J. Mater. Process. Technol. 125-126, 764–771. doi:10.1016/S0924-0136(02)00387-4.

Trzepieciński, T., Bazan, A., Lemu, H.G., 2015. Frictional characteristics of steel sheets used in automotive industry. Int. J. Automot. Technol. 16, 849–863. doi:10.1007/s12239-015-0087-1.

Xu, D., Chen, J., Tang, Y., Cao, J., 2012. Topology optimization of die weight reduction for high-strength sheet metal stamping. Int. J. Mech. Sci. 59, 73–82. doi:10.1016/j.ijmecsci.2012.03.006.

Yoon, J.W., Lou, Y., Yoon, J., Glazoff, M.V., 2014. Asymmetric yield function based on the stress invariants for pressure sensitive metals. Int. J. Plast. 56, 184–202. doi:10.1016/j.ijplas.2013.11.008.

Yoshida, F., Uemori, T., 2002. A model of large-strain cyclic plasticity describing the Bauschinger effect and workhardening stagnation. Int. J. Plast. 18, 661–686. doi:10.1016/S0749-6419(01)00050-X.

Zavarise, G., De Lorenzis, L., 2009. The node-to-segment algorithm for 2D frictionless contact: classical formulation and special cases. Comput. Methods Appl. Mech. Eng. 198, 3428–3451. doi:10.1016/j.cma.2009.06.022.